Diagnosis of decadal predictability of Southern Ocean sea surface temperature in the GFDL CM2.1 model

Liping Zhang[1& 2], Thomas L. Delworth[2], and Liwei Jia[1&2]

[1]Atmospheric and Oceanic Science
Princeton University
New Jersey, U.S.

[2]NOAA/Geophysical Fluid Dynamics Laboratory, Princeton
New Jersey, U.S.

Revised to JC
Oct, 2016

Corresponding author address: Liping Zhang, NOAA/Geophysical Fluid Dynamics Laboratory, 201 Forrestal Rd., Princeton, NJ 08540. E-mail: Liping.Zhang@noaa.gov

Abstract

The average predictability time (APT) method is used to identify the most predictable components of decadal sea surface temperature (SST) variations over the Southern Ocean (SO). These components are identified from a 4000 year unforced control run of the GFDL CM2.1 model. The most predictable component shows significant predictive skill for periods as long as 20 years. The physical pattern of this variability has a uniform sign of SST anomalies over the SO, with maximum values over the Amundsen-Bellingshausen-Weddell Seas. Spectral analysis of the associated APT time series shows a peak on time scales of 70-120 years. This most predictable pattern is closely related to the mature phase of a mode of internal variability in the SO that is associated with fluctuations of deep ocean convection. The second most predictable component of SO SST is characterized by a dipole structure, with SST anomalies of one sign over the Weddell Sea and SST anomalies of the opposite sign over the Amundsen-Bellingshausen Seas. This component has significant predictive skill for periods as long as 6 years. This dipole mode is associated with a transition between phases of the dominant pattern of SO internal variability. The long time scales associated with variations in SO deep convection provide the source of the predictive skill of SO SST on decadal scales. These analyses suggest that if we could adequately initialize the SO deep convection in a numerical forecast model, the future evolution of SO SST and its associated climate impacts is potentially predictable.

1. Introduction

Over the past decade, the observed sea surface temperature (SST) in the Southern Ocean (SO) did not increase (e.g., Latif et al. 2013; Zhang et al. 2016), but instead exhibited cooling anomalies. The associated Antarctic sea ice extent showed an expansion, with a record maximum occurring in September 2012 (e.g., Cavalieri and Parkinson 2008; Comiso and Nishio 2008). In the meantime, the Southern Ocean subsurface (below 500m) warmed considerably (Purkey and Johnson 2010, 2012). The slowdown in the rate of SO warming can't be attributed to a decrease in greenhouse-gas emission from human activity. Climate models forced by observed temporally varying radiative forcing do not reproduce the observed cooling around the Antarctic, but instead simulate a slow but steady warming and Antarctic sea ice loss (Purich et al. 2016). It is therefore likely that internal variability is contributing to the declining SSTs in the SO (Cane 2010; Zunz et al. 2012; Polvani and Smith 2013). However, the extent to which such SO internal climate variability can be simulated and hence predicted on decadal timescales is still not known.

Decadal predictions are in high demand by decision makers who help plan infrastructure investments and resource rearrangements (Cane 2010). The scientific basis of decadal prediction should be built firmly before this demand can be met. A first step is to estimate whether there is a potentially predictable component on decadal scales. Decadal predictability is commonly estimated by two approaches: prognostic and diagnostic approaches (e.g., Pohlmann et al. 2004). In the prognostic approach, decadal predictability is evaluated based on an atmosphere-ocean fully coupled model (AOGCM) initialized by identical oceanic and perturbed atmospheric conditions. The spread within the ensemble is interpreted as an estimate of predictability. Previous studies further extend this method to decadal hindcasts/forecasts that are initialized with observations. The prediction skill is assessed by how close the time evolving variable produced by the initialized model matches the observation. The assumption is that the coupled model could be realistically initialized with three-dimensional observational fields. However, this is frequently not possible, particularly over the SO where long term observations are rare. Thus, pioneering studies using prognostic method primarily focused on the North Atlantic and North Pacific Oceans where the observations are more numerous and can better be used for model initialization (Keenlyside et al. 2008; Smith et al. 2007; Robson et al. 2012; Yeager et al. 2012; Yang et al. 2013; Msadek et al. 2014; Mochizuki et al. 2010; Meehl and Teng, 2012). These model results suggested that the observation-based initial conditions improve skill in the North Atlantic and, to a lesser extent, North Pacific.

Compared to prognostic approaches, the diagnostic approaches are easier to carry out since they don’t require extensive data for initializing prediction models. Diagnostic predictability can be evaluated by various statistical methods, including examining eigenmodes of a linear inverse model (LIM) (Newman 2007), examining the growth of optimal perturbations (Zanna et al. 2012) and investigating the potential predictability variance fraction (ppvf) (Boer 2004; 2011). These statistical tools can identify where and on what time scale the variables have potential high predictability.

Using multi-model ensemble data participating in the Coupled Model Intercomparison Project (CMIP), Boer (2004) found that the largest potential predictability on decadal scales is predominately over the high-latitude oceans, particularly in the SO and North Atlantic. These diagnostic approaches might serve as a useful benchmark for decadal predictions that are based on observation-initialized numerical models.

Given the dearth of long term observations over the SO, we choose to use a diagnostic method to investigate the potential predictability of decadal-scale SO SST variations by taking advantage of a long control integration of the GFDL CM2.1 model. The decadal-scale SO SST variability found in CM2.1 model has great similarities to that shown in Latif et al. (2013) and Wang and Dommenget (2016). The method we used here is called average predictability time (APT), as proposed by DelSole and Tippett (2009a, b). The APT method finds the most predictable patterns. One advantage of this technique is that it can capture predictable features that contribute little to total variance growth or cannot be expressed as oscillatory modes (DelSole et al. 2013). The main goal of the current study is to examine the leading predictable components of SO SST and the associated climate impacts within a long control simulation of the GFDL CM2.1 model. The physical processes contributing to this predictability are also investigated. We hope our diagnostic analysis can provide a useful reference point for future SO decadal forecasts using observation-initialized numerical models.

The rest of the paper is organized as follows: We briefly describe the CM2.1 model, ppvf and APT methodologies in section 2. In section 3, the potential predictability of SO SST using both ppvf and APT methods is presented. In section 4, we explore the physical mechanisms that give rise to high decadal predictability over the SO. The multiyear predictability of SO SST related climate impacts over the Antarctic continent is examined in section 5. The paper concludes with a discussion and summary in section 6, including a comparison of results found with CM2.1 to results from another GFDL climate model, CM3.

2. Models and Methods

a. Coupled Model

The long-time integrated control run we used in the present paper comes from the Geophysical Fluid Dynamics Laboratory (GFDL) Coupled Model version 2.1 (CM2.1, Delworth et al. 2006). The CM2.1 model has an atmospheric horizontal resolution of $2^{o}\times 2^{o}$, with 24 levels in the vertical. The ocean and ice models have a horizontal resolution of 1^{o} in the extratropics, with meridional grid linearly decreasing to $1/3^{o}$ near the equator. The ocean model has 50 levels in the vertical, with 22 evenly spaced levels over the top 220 m. A 4000 year control simulation is conducted with atmospheric constituents and external forcing held constant at 1860 conditions. We perform analyses using the last 3000 years of the simulation (1001-4000yr) to avoid initial model drift. All data are linearly detrended before analysis. Characteristics of the model's Antarctic bottom water and its relationship with the Weddell Gyre have previously been described (e.g., Zhang and Delworth, 2016). The impact of multi-decadal Atlantic meridional overturning circulation (AMOC) variations on the SO using this model was also described in Zhang et al. (2016). The realism of the model characteristics as described in these previous studies provides some level of confidence that this model is an appropriate tool for studies of the model predictability of SO.

b. Methods

We first use the potential predictability variance fraction (ppvf) (Boer 2004; 2008) to give general information about the high predictability regions. Boer (2004) suggested that the total climate variability (σ^2) can be decomposed into the slow time scale "potentially predictable" component (${\sigma_L}^2$) and unpredictable climate noise (${\sigma_\varepsilon}^2$). The ppvf is therefore defined as a fraction of long time scale (or low frequency) variability with respect to the total variability (ppvf $= {\sigma_L}^2/\sigma^2$). ${\sigma_L}^2$ is the variance of m-year mean SST, where m can be selected as any integer number. The high ppvf regions identify those areas in which long timescale variability stands out clearly from short timescale variability, and thus variability in these regions may be at least potentially predictable.

We then use the APT method to derive leading predictable components over these high ppvf regions. A standard measure of predictability (DelSole and Tippett 2009b) is defined as:

$$\mathrm{P}(\tau) = \frac{{\sigma_\infty}^2 - {\sigma_\tau}^2}{{\sigma_\infty}^2} \ , \qquad (1)$$

where $\sigma_\infty{}^2$ is climatological variance and $\sigma_\tau{}^2$ is the ensemble forecast variance at lead time τ. This measure is close to 1 for a perfect forecast and close to zero when the ensemble forecast spread approaches the climatological spread.

The APT is defined as the integral of predictability over all lead times:

$$\mathrm{APT} = 2\sum_{\tau=1}^{\infty}\left(\frac{\sigma_\infty{}^2 - \sigma_\tau{}^2}{\sigma_\infty{}^2}\right). \qquad (2)$$

It is an integral measure of predictability and thus is independent of lead time. To maximize APT, we seek an inner product $\mathbf{q}^{\mathrm{T}}\mathbf{x}$, where $\mathbf{q}$ is a projection vector, $\mathbf{x}$ is the state vector and superscript T denotes the transpose operation. The component $\mathbf{q}^{\mathrm{T}}\mathbf{x}$ has respective forecast and climatological variances,

$$\sigma_\tau{}^2 = \mathbf{q}^{\mathrm{T}} \textstyle\sum_\tau \mathbf{q} \qquad \text{and} \qquad \sigma_\infty{}^2 = \mathbf{q}^{\mathrm{T}} \textstyle\sum_\infty \mathbf{q}. \quad (3)$$

Substituting (3) into (2) generates

$$\mathrm{APT} = 2\sum_{\tau=1}^{\infty}\left(\frac{\mathbf{q}^{\mathrm{T}}(\sum_\infty - \sum_\tau)\,\mathbf{q}}{\mathbf{q}^{\mathrm{T}}\sum_\infty \mathbf{q}}\right). \qquad (4)$$

DelSole and Tippett (2009b) and Jia and DelSole (2011) pointed out that maximizing APT leads to an eigenvalue problem

$$2\sum_{\tau=1}^{\infty}\left(\textstyle\sum_\infty - \sum_\tau\right)\mathbf{q} = \lambda \textstyle\sum_\infty \mathbf{q}. \qquad (5)$$

Since the control run data we used here only has a single ensemble member, a linear regression model is adopted to estimate APT . The regression model is written as

$$\hat{\mathbf{x}}_{t+\tau} = \mathbf{L}_\tau \mathbf{x}(t) + \epsilon(t), \qquad (6)$$

where $\mathbf{x}(t)$ denotes the predictor at time τ, $\hat{\mathbf{x}}_{t+\tau}$ is the predictand at time $t+\tau$, $\mathbf{L}_\tau$ is the regression coefficient at time τ and $\epsilon(t)$ is the residual term. The climatological and forecast and matrices thus have the form of

$$\sum_{\infty} = \mathbf{C}_0 \quad and \quad \sum_{\tau} = \mathbf{C}_0 - \mathbf{C}_\tau \mathbf{C}_0^{-1} \mathbf{C}_\tau^T, \qquad (7)$$

where $\mathbf{C}_\tau$ is the time-lagged covariance matrix and $\mathbf{C}_0$ is the climatological variance. Substituting (7) into the eigenvalue problem (5) gives

$$\left(2 \sum_{\tau=1}^{\infty} \mathbf{C}_\tau \mathbf{C}_0^{-1} \mathbf{C}_\tau^T\right)\mathbf{q} = \lambda \mathbf{C}_0 \mathbf{q}, \qquad (8)$$

The left term in (8) represents the integration of signal covariance, while the right term represents the total climatological covariance in which λ and $\mathbf{q}$ denote the eigenvalue and projection vector, respectively.

When we apply this method to our control simulation, both the predictors and predictands are projected on the leading 30 Principal components (PCs). The resulting 3000-yr length PCs are then split in half, as also seen in Jia and DelSole (2011). The first 1500 year data from the control run, called training data, are used to maximize APT in equation (8), and the second 1500 year are kept for verification. As suggested by DelSole and Tippett (2009b), we use the squared multiple correlation R_τ^2 to estimate the potential predictability. R_τ^2 can represent the amount of variation in the predictand that is accounted for by the variation in the predictors and has a form of

$$R_\tau^2 = \frac{\mathbf{q}^T \mathbf{C}_\tau \mathbf{C}_0^{-1} \mathbf{C}_\tau^T \mathbf{q}}{\mathbf{q}^T \mathbf{C}_0 \mathbf{q}}. \qquad (9)$$

The $\mathbf{q}$ is calculated from the training data, while the covariance terms $\mathbf{C}_\tau$ and $\mathbf{C}_0$ are obtained from verification data. In general, the slower decrease of R_τ^2 with lead time, the larger potential predictability. The statistical significance of APT is examined by Monte Carlo experiments. We generate two independent random matrices that have zero mean and unit variance and apply them to equation (8) to produce an ordered sequence of optimized APT values. This procedure is then repeated 100 times and the

95% eigenvalue from (8) was selected. If the APT value computed from training data exceeds the 95% value from the Monte Carlo experiments, the null hypothesis (white noise, unpredictable) will be rejected and the APT value from training data is significant at 5% significance level.

3. Potential predictability over the Southern Ocean

a. High predictability regions

Fig. 1 shows the ppvf of 5-yr, 11-yr and 25-yr mean SST over the global oceans in CM2.1 model. In agreement with previous studies (e.g., Boer 2004; Boer and Lambert 2008), high latitude regions exhibit relatively higher potential predictability than the middle and low latitudes. This contrast becomes more obvious when the averaging scale increases from 5-yr to 11-yr (Fig. 1a versus Fig. 1b). The potential predictability of 11-yr mean SST is primarily concentrated in the North Atlantic, North Pacific and SO, with comparable magnitudes in both hemispheres (Fig. 1b). When we consider the 25-yr mean SST, the SO potential predictability is even higher than the North Atlantic and North Pacific Oceans (Fig. 1c). The large values of ppvf over the SO in GFDL model indicate that the long timescale variability over the SO is very pronounced.

b. APT analysis of SO SST

We identify the leading predictable components of SO SST using standard APT analysis. The analyzed area is from 35^{o}S to 80^{o}S and from 0^{o}E to 360^{o}E. Note that the results are not sensitive to the northern boundary choices, as long as the latitude is within the Southern Hemisphere (not shown). The leading two components have significant APT values at 5% significance level. The SST spatial pattern associated with the most predictable component (APT1) has loadings of the same sign over the SO, with maximum anomalies over the Amundsen-Bellingshausen-Weddell Seas (Fig. 2a). The APT value for this mode is 20.6 years. The corresponding time series of APT1 shows prominent multi-decadal fluctuations (Fig. 2b), with a spectral peak around 70-120 years (Fig. 2c). The squared multiple correlation R^2 of the leading predictable component as a function of time lag derived from independent control run is further shown in Fig. 2d. The R^2 above the 95% confidence level denotes significant predictability. This figure shows that the APT1 mode has potential predictability up to 20 years. The traditional and damped persistence forecasts, which assume the forecast equals the initial condition and forecast decays exponentially in time, respectively, are shown in Fig. 2d as well. It can be seen that the skill arising from APT maximization is higher than both persistence forecasts.

The second most predictable component (APT2) of SO SST is characterized by a dipole structure, with SST anomalies of one sign over the Weddell Sea and SST anomalies of the opposite sign in the Amundsen-Bellingshausen Seas (Fig. 3a). The associated time series has a pronounced multi-decadal oscillation, but is quite noisy compared to APT1 (Fig. 3b versus Fig. 2b). The power spectrum of APT2 time series reveals a quasi-70-120 year peak (Fig. 3c) that also appears in APT1 (Fig. 2c). Fig. 3c also shows substantial variances are distributed in the 2-50 year frequency bands in the APT2 power spectrum, in sharp contrast to APT1 (Fig. 2c). This leads to a relatively small variance fraction in 70-120 year frequency bands and thus a noisy

APT2 time series. The R^2 of this second most predictable component indicates a potential predictability up to 5 years (Fig. 3d), which is much shorter than the first predictable mode due to noisy characteristics. The APT2 predictability is only slightly higher than the persistence forecasts (Fig. 3d), suggesting that the skill mainly arises from the SST persistence.

The coherent spectrum of APT1 and APT2 time series shows high coherences over their common peak period 70-120yr (Fig.4a), suggesting that the leading two predictable components may have the same ocean origin. To confirm our hypothesis, we conduct a lead lag correlation analysis between these two time series (Fig. 4b). As expected, the simultaneous correlation is zero due to the orthogonality of the APT decomposition. Significant positive (negative) correlations are found when the APT1 leads (lags) APT2 by 10-30 years. These lead and lag times account for approximately a quarter of the APT1/APT2 period (70-120 year). These phenomena imply that the two predictable components are very likely quadrature related.

4. Ocean origin of high decadal predictability of SO SST

a. Climate fluctuations associated with leading predictable modes

To understand the physical processes associated with the leading predictable components, we regress several important variables onto the APT1 and APT2 time series, respectively (Fig. 5 and 6). Fig. 5a exhibits the surface net heat flux and mixed layer depth (MLD) anomalies associated with the APT1 time series. The SO experiences broad negative heat flux anomalies that tend to damp positive surface temperature anomalies. This implies that the uniform SO SST warming in APT1 originates from the ocean dynamics, instead of atmosphere forcing. The MLD change shown in Fig. 5a displays a strong positive anomaly over the Weddell Sea, indicating strong deep convection there. Note that the long term mean global meridional overturning circulation (GMOC) has a negative value south of 60^{o}S, which represents an anticlockwise cell that denotes the strength of Antarctic Bottom water (AABW) formation as well as deep convection (Fig. 7a). Fig. 5b shows prominent negative GMOC anomalies south of 20^{o}S, suggesting a strengthening and northward extension of the AABW Cell. In the mean state the subsurface is warmer than the surface in the region of the SO. Therefore, the spin up of AABW cell drives a subsurface-surface temperature dipole in the SO, with a cooling anomaly in the subsurface and a warming anomaly at the surface (Fig. 5c) that corresponds to a decrease of Antarctic sea ice (Fig. 5d). The surface wind is characterized by a zonally-oriented anticyclone around 40^{o}S-60^{o}S band, which is very likely due to local SST feedback (Zhang et al. 2016). These ocean and atmosphere variabilities associated with the APT1 mode are consistent with the SO centennial climate variability found in Kiel Climate Model (Latif et al. 2013).

The heat flux and MLD anomalies associated with the APT2 time series show opposite signs with the APT1 (Fig. 6a versus Fig. 5a), suggesting a weakening of deep convection over the Weddell Sea. Accordingly, the GMOC anomaly shows a spin down of AABW cell (Fig. 6b). Compared to APT1, the GMOC change is relatively weak and mainly confined south of 60^{o}S (Fig. 5b versus Fig. 6b). The associated zonal mean temperature shows a weak cold surface-warm subsurface dipole structure over the SO (Fig. 6c). In contrast to the uniform sea ice response in APT1, the sea ice change associated with APT2 exhibit a dipole pattern, with sea ice increase in the Weddell Sea and sea ice decrease over the Amundsen-Bellingshausen Seas (Fig. 6d). The sea ice anomaly over the Amundsen-Bellingshausen Seas is not only related to the SST anomalies but also linked with the surface wind. As shown in Fig. 6d, there is an anticyclonic wind around 160^{o}-40^{o}W over the SO, which corresponds to a northwest wind anomaly over the Amundsen-Bellingshausen Seas. The northwest wind favors poleward warm temperature advection and thus a decrease of sea ice there.

The above regression analyses suggest that the leading two predictable components of SO SST are very likely to be associated with deep convection changes. To test this hypothesis, we examine the SO deep convection characteristics in the CM2.1 model. As mentioned above, we use the AABW cell anomaly to represent the SO deep convection fluctuations. The strength of the AABW cell each year is defined as the minimum value of the streamfunction south of 60^{o}S (Fig. 7a). Note that if the AABW cell index is a negative anomaly, which means a strong overturning cell. The time series of AABW cell index (Fig. 7b) has pronounced multi-decadal variabilities at 70-120yr time scales (Fig. 7c) which coincide with the typical period peaks of APTs (Fig. 7c versus Fig. 2c and Fig. 3c). We also show in Fig. 7d the lead lag correlation between the AABW cell index and APT1 time series. It shows a negative correlation as low as -0.6 when the AABW leads the APT1 by about 5 years. Since the

APT1 and APT2 time series are in quadrature, significant correlations are also found between the AABW index and APT2 with some time lags (not shown).

b. Southern Ocean multi-decadal variability

To further confirm the close relationship between the leading predictable components and SO deep convection, we show in Fig. 8 the multi-decadal cycle of AABW cell. The AABW cell cycle is obtained by the lagged regression of GMOC anomalies upon the AABW cell index. To focus on multi-decadal variability, all data are first 10-yr averaged prior to regression. At a lag of 0yr, the AABW cell is in its mature positive phase, with a maximum increase south of 60^{o}S and a northward extension to 40^{o}S (Fig. 8a). We characterize the evolution of the AABW cell cycle by the regression coefficients at various lags. As we move forward from lag 0, the GMOC anomalies south of 60^{o}S gradually weaken, while the northward extension becomes stronger and stronger (Fig. 8b-d). The GMOC negative anomalies extend to about 20^{o}N at a lag of 15yr (Fig. 8d). At a lag of 20yr, a positive GMOC anomaly emerges south of 60^{o}S. This positive GMOC anomaly then intensifies and gradually spreads northward, which in turn weakens the negative GMOC anomaly in the north (Fig. 8e-j). At a lag of 45yr, the AABW phase is totally flipped and reaches its mature negative phase (Fig. 8j). A close examination finds that the spatial structure of quasi mature phase of AABW cell (Fig. 8a, b) closely resembles the GMOC anomalies associated with the APT1 (Fig. 5b). Similarly, the transition phase of AABW cycle (Fig. 8f) matches with the GMOC anomalies associated with the APT2 very well (Fig. 6b).

We show in Fig. 9 the multidecadal SST cycle associated with the deep convection. During the AABW cell mature positive phase, the SO experiences broad warming anomalies, with maximum values over the Weddell Sea (Fig. 9a, b). The warm SST over the SO corresponds to a zonally-oriented anticyclone wind, with easterly anomalies around 40^{o}S and westerly anomalies at 75^{o}S. We note that the mature phase of the SO SST cycle here is in good agreement with the SST pattern in APT1 (Fig. 9a, b versus Fig. 2a). Accompanied with the AABW cell weakening south of 60^{o}S (Fig. 8a-d), the positive SST anomalies over the Weddell Sea gradually weaken (Fig. 9a-d). At the same time, the Southeast Pacific SST warming gradually spreads to the equator through the fast positive wind-evaporation-SST (WES) feedback and slow weakening of subtropical cell (e.g., Zhang et al. 2011) (Fig. 9a-d). Once the warm SST anomaly reaches the equatorial eastern Pacific, it triggers the tropical positive Bjerknes feedback to further amplify the initial SST anomaly. The warm SST anomaly over the tropical Pacific induces the positive phase of Pacific North America (PNA) teleconnection (e.g., Horel and Wallace 1981) and Pacific South America (PSA) teleconnection (Mo and Higgins 1997) as well. The PNA teleconnection leads to a PDO-like (e.g. Zhang and Delworth, 2015, 2016) SST pattern over the North Pacific with cold SST anomalies over the western and central Oceans (Fig. 9b-d). The PSA teleconnection induces a wavenumber 3 in the mid-latitude, with an anticyclonic circulation over the Amundsen-Bellingshausen Seas that favors warm poleward advection and thus warm SST there (Fig. 9c-d). At a lag of 20yr, a cooling SST anomaly appears in the Weddell Sea (Fig. 9e) resulting from the emergence of a negative AABW cell shown in Fig. 8e. The SST over the SO is characterized by a dipole pattern at this moment, with a warm SST in the Amundsen-Bellingshausen Seas and a cold SST in the Weddell Sea. The negative SST anomaly in the Weddell Sea further grows in the Weddell Sea and then extends to the entire SO (Fig. 9f-j). At lags of 35-45yr, the SO is almost covered by the negative SST anomalies (Fig. 9h-j), which reaches to the opposite phase of deep convection. We note again that the transition phase of SO SST cycle matches very well with the SST pattern in APT2 (Fig. 9f versus Fig. 3a). These SST pattern similarities suggest that the leading two predictable components of SO SST originate from the internal multi-decadal cycle of SO deep convection. The first component arises from the quasi mature phase of deep convection, while the second component is contributed from the transition phase of deep convection.

The associated sea ice and subsurface temperature variabilities (Fig. 10, 11) are physically consistent with our previous analyses. The sea ice primarily follows the SST changes, with a cold (warm) SST anomaly corresponding to a sea ice increase (decrease). Thus, the mature positive phase sea ice at lag 0yr is characterized by a sea ice decrease over the SO (Fig. 10a, b), whereas the transition phase sea ice at lag 25yr exhibits a sea ice decrease in the Amundsen-Bellingshausen Seas and a sea ice increase in the Weddell Sea (Fig. 10f). These sea ice characteristics are consistent with the sea ice anomalies associated with the APT1 and APT2 (Fig. 10a, b versus Fig. 5d; Fig. 10e, f versus Fig. 6d). Fig. 11 shows the multidecadal zonal mean temperature cycle. As expected, the temperature response agrees with the deep convection change (Fig. 11 versus Fig. 8). The spin up (spin down) of AABW cell brings subsurface warm water to the surface, thereby leading to a warm (cold) SST in the surface and a cold (warm) temperature in the subsurface. The dipole temperature weakens as the AABW cell spins down and vice versa. The temperature dipole structure becomes quite weak during the deep convection transition phase as compared to the mature phase (Fig. 11f versus Fig. 11a). Again, these zonal mean temperature anomalies in the mature and transition phases match with the temperature responses in APT1 and APT2, respectively (Fig. 11a, b versus Fig. 5c; Fig. 11f versus Fig. 6c).

We note that the most predictable SST (APT1) time series over the SO lags the AABW cell index by about 5 years (Fig. 7d). The delayed SST response primarily arises from the slow adjustment of the ocean that consists of advection/wave propagation (Zhang and Delworth 2016), which is also seen in the CM2.1 fully coupled control run. Fig. 12a exhibits the SO (50^o-75^oS, 0^o-360^oE) area averaged SST time series, the Weddell Sea (75-55^oS, 52^oW-30^oE) area averaged SST time series as well as the AABW cell index. Their lead-lag correlations are shown in Fig. 12b. All three indices have pronounced multi-decadal fluctuations and they are highly correlated. The AABW cell index is simultaneously correlated with the local (Weddell Sea) SST due to strong deep convection there. In contrast, the maximum correlation between the AABW cell index and remote SO SST occurs when the AABW cell leads by about 5 years (Fig. 12b). The delayed SST response is again related to the slow ocean adjustment.

c. Mechanisms contributing to SO multi-decadal variability

The main driver of the deep convection in CM2.1 model is the heat reservoir at mid-depth and its recharge process, which have great similarities with that in Kiel Climate model (Martin et al. 2013). Fig. 13a shows the time evolution of annual mean vertical temperature anomaly averaged over the Weddell Sea. The temperature anomaly is relative to a composite of 30 years of two major convection periods (year 2950-2980 and year 3020-3050). During active convection, the temperature distribution is almost homogeneous over the entire water column. However, the heat tends to accumulate at mid-depth when the convection stops. The heat spreads over time, warms the entire water column below 300m, destabilizes the ocean stratification, and eventually triggers the occurrence of deep convection.

The heat at mid-depth over the Weddell Sea primarily comes from the northern subtropics. Before the shutdown of deep convection, the westward return flow in the southern branch of the Weddell Gyre effectively drags heat into the Weddell Sea (Fig. 13b). This strong barotropic clockwise gyre exists over almost the entire water column and its' strength is strongly associated with the deep convection itself due to interactions between the AABW outflow and topography (Zhang and Delworth 2016). The gyre still exits when the convection spins down, albeit with a weak amplitude (Fig. 13c).

The convection shutdown is the depletion of heat reservoir at mid-depth (Fig. 13a). The deep convection leads to a heat depletion in the entire Atlantic and Indian Ocean Basins (Fig. 13d). By separating the heat content into upper 1000m and deep components, we can see the deep ocean loses and the upper ocean gains heat when the convection occurs and vice versa (Fig. 13e, f). Moreover, the deep ocean heat content dominates the whole water column heat changes. Most of the heat lost during the deep convection is imported into the Weddell Sea by the westward return flow of the Weddell Gyre (Fig. 13b).

In brief, the recharge/discharge processes of heat reservoir at mid-depth are the main mechanism driving multi-decadal variability over the SO, although other processes such as heat flux loss to the atmosphere, freshwater change in the surface and sea ice melt/formation could slightly modulate this variability (not shown). The timescale of the cycle is largely determined by the recharge and discharge processes of the heat reservoir over the Weddell Sea. The heat content variation there is associated with the warm water in the northern subtropics and the Weddell Gyre strength.

5. Climate impacts

In this section, we examine the potential multiyear predictability of surface air temperature (SAT) and precipitation over the Antarctic continent. We find the multiyear predictability of land variables using land predictor itself is lower than the predictability using global SST (not shown). This suggests that the land predictability on interannual-to-decadal time scales is primarily driven by SST (Hoerling and Kumar 2003; Held et al. 2005). Thus, we use a generalized APT method (GAPT) (Jia and DelSole 2011), which is similar to the standard APT described in section 2, except that the predictor and predictand are two different variables. Here the predictor is global SST, while the predictand is SAT or precipitation.

We show in Fig. 14 the most predictable component of SAT over the Antarctic Continent. The SAT physical pattern has a uniform warming over the entire Antarctic land, with maximum amplitudes over the Antarctic Peninsula (Fig. 14a). The R^2 values in the verification data suggest that the Antarctic SAT is able to be predicted 6 years in advance (Fig. 14c). The SAT time series has a pronounced 70-110-yr peak (Fig. 14b), implying a potential linkage with the SO deep convection. The SST regression pattern associated with the APT1 time series shows notable SST warming over the SO, with negligible signals over the Northern Hemisphere (Fig. 14d). The maximum SST warming occurs over the Weddell Sea where deep convection dominates. This SST pattern highly resembles the mature phase SST associated with the deep convection fluctuations (Fig. 14d versus Fig. 9a). Thus, we conclude that the most predictable SAT over the Antarctic continent results from the SO SST memory that is controlled by the deep convection activity.

Similar to the SAT, the most predictable component of precipitation over the Antarctic continent primarily arises from the prediction skill of SO SST that is closely linked with SO deep convection. The physical pattern of precipitation displays positive anomalies over land where the adjacent SO has significant SST warming (Fig. 15a versus Fig. 15d). The power spectrum of the GAPT1 time series, again, shows a similar frequency peak with the SO SST and AABW cell (Fig. 15b versus Fig. 2c and Fig. 7d). The R^2 values of precipitation are lower than that of SAT due to the noisy characteristics of precipitation (Fig. 14c versus Fig. 15c). However, the potential predictability of precipitation can still be up to 4 years (Fig. 15c).

6. Summary, discussion and conclusion

By taking advantage of the GFDL CM2.1 4000-yr control run integration, we investigate the potential decadal predictability of SO SST in the present paper. We use a new statistical optimization technique, called APT analysis (DelSole and Tippett 2009a, b), to identify the leading predictable components of SO SST on decadal time scales. The APT analysis maximizes an integrated prediction variance obtained from a linear regression model, in which both the predictor and predictand are SST. Note that the long term control integration does not include anthropogenic forcing or changes in natural forcing from volcanoes or interannual variations of solar irradiance. The potential predictability shown here is therefore purely from internal variability.

The most predictable component of SO SST can be predicted in an independent verification data by a linear regression model, with significant skill up to 20 years. The predictable pattern has a uniform SST sign over the SO, with maximum values over the Amundsen-Bellingshausen-Weddell Seas. The associated APT time series has a 70-120-yr spectral peak. This predictable pattern is closely related to the mature phase of the SO internal variability that originates from deep convection fluctuations. In the CM2.1 model, deep convection mainly occurs over the Weddell Sea and has multidecadal fluctuations on a 70-120-yr time scale. This multi-decadal timescale selection is largely associated with the discharge and recharge processes of heat reservoir in the deep ocean. Slow subsurface ocean processes provide long time scales that give rise to decadal predictability of SO SST. The SO SST has significant climate impacts on the SAT and precipitation over the Antarctic continent. The SAT and precipitation can be potentially predictable up to 6yr and 4yr in advance, respectively. These multiyear prediction skills arise from the SO SST, which is again attributed to the internal deep convection fluctuations over the Weddell Sea.

The second most predictable component of SO SST is characterized by a dipole structure, with SST anomalies of one sign over the Weddell Sea and SST anomalies of the opposite sign over the Amundsen-Bellingshausen Seas. This component has statistically significant prediction skill for 6 years based on a linear regression model. A close examination reveals that this dipole mode primarily arises from the transition phase of the dominant pattern of SO internal variability. Again, the slow ocean memory associated with the SO deep convection provides the multiyear prediction skill of this second most predictable component. Interestingly, this second component corresponds to a sea ice dipole structure over the Amundsen-Bellingshausen-Weddell Seas, which somewhat resembles the observed sea ice trend in recent years (e.g., Li et al. 2014). The associated surface wind over the SO characterized by a cyclone (or anticyclone) around 160^{o}-40^{o}W favors sea ice dipole formation, which is also consistent with what was found in observation. These similarities provide a hypothesis that some prominent trends observed during the recent decades in the Southern Hemisphere may have some contributions from internal variability in the SO that is strongly associated with deep convection fluctuations.

In order to provide some perspective on the robustness of our results, we perform the same APT diagnostics on a long control integration of a different GFDL climate model, CM3 (Donner et al., 2011). The CM3 model has an ocean component that is quite similar to CM2.1, but the atmospheric component of CM3 has substantial differences from CM2.1. Similar to CM2.1, the most predictable SST pattern in CM3 displays a uniform sign over the SO, while the second most predictable SST pattern shows a dipole structure (Fig. 16a, b). The maximum SST centers associated with these two modes are primarily over continental shelfs of the Weddell and Ross Seas (Fig. 16a and b), which are somewhat different from CM2.1 (Fig. 2 and 3). These SST center differences are largely associated with the deep convection position in two models (not shown). The SO deep convection mainly occurs in the Weddell Sea in CM2.1 model, including both open oceans and continental shelf. In contrast, the deep convection in CM3 model takes places in continental shelfs of the Weddell and Ross Seas.

The power spectrum of APT1 and APT2 time series in CM3 model shows prominent spectrum peaks around 300 years, which are longer than that in CM2.1 model (Fig. 16c versus Fig. 2c and 3c). This leads to a long persistence time of SST and therefore a long predictability skill, as presented in Fig. 16d and e. The predictive skill can be up to 30 years for APT1 component and 10 years for APT2 mode. In agreement with that in the CM2.1 model, these leading predictable components are found to be closely linked with the SO deep convection fluctuations (Fig. 16f).

Our diagnostic approaches for the decadal predictability of SO SST in the current paper suggest that if we could correctly initialize the SO deep convection in the numerical forecast model, the future evolution of SO SST and its associated climate impacts might be predictable on decadal scales. Such predictions would ideally be performed using models with simulations of the SO that are as realistic as possible. In addition, enhanced ocean observations, particularly subsurface observations over the far SO, are also needed to characterize the state of the SO. An important caveat is that the realism of model's simulation of the SO will impact how relevant such potential predictive skill is for predictions of the real climate system. The decadal prediction skill of SO SST based on real decadal hindcasts/forecasts is currently under investigation and will be the topic of a forthcoming paper.

Acknowledgement:

We are grateful to Soyna Legg and Carolina O. Dufour for their constructive comments on an early version of the paper. The work of T. Delworth is supported as a base activity of NOAA’s Geophysical Fluid Dynamics Laboratory. L. Zhang and L. Jia are supported through Princeton University under block funding from NOAA/GFDL.

Reference:

Boer, G. J., 2004: Long time-scale potential predictability in an ensemble of coupled climate models. *Climate Dyn*., **23**, 29-44.

Boer, G. J., 2011: Decadal potential predictability of twenty-first century climate. *Climate Dyn*., **36**, 1119-1133.

Boer, G. J., and S. J. Lambert, 2008: Multi-model decadal potential predictability of precipitation and temperature. *Geophys. Res. Lett.*, **35**, L05706, doi:10.1029/2008GL033234.

Cane, M. A., 2010: Climate science: Decadal predictions in demand. *Nat. Geosci.*, **3**, 231–232.

Cavalieri, D. J., and C. L. Parkinson, 2008: Antarctic sea ice variability and trends, 1979-2006. *J. Geophys. Res.*, **113**, C07004, doi:10.1029/2007JC004564.

Chen, X., and K.-K. Tung, 2014: Varying planetary heat sink led to global-warming slowdown and acceleration. *Science*, **345**, 897–903.

Comiso, J. C., and F. Nishio, 2008: Trends in the sea ice cover using enhanced and compatible AMSR-E, SSM/I, and SMMR data. *J. Geophys. Res.*, **113**, C02S07, doi:10.1029/2007JC004257.

DelSole, T., and M. K. Tippett, 2009a: Average predictability time. Part I: Theory. *J. Atmos. Sci.*, **66**, 1172–1187.

DelSole, T. , and M. K. Tippett, 2009b: Average predictability time. Part II: Seamless diagnosis of predictability on multiple time scales. *J. Atmos. Sci.*, **66**, 1172–1187.

DelSole, T., L. Jia, and M. K. Tippett, 2013: Decadal prediction of observed and simulated sea surface temperatures. *Geophys. Res. Lett.*, **40**, 2773–2778, doi:10.1002/grl.50185.

Delworth, T. L., and Coauthors, 2006: GFDL's CM2 global coupled climate models. Part I: Formulation and simulation characteristics. *J. Climate*, **19**, 643–674.

Donner, L. J., and coauthors, 2011: The dynamical core, physical parameterizations, and basic simulation characteristics of the atmospheric component AM3 of the GFDL global coupled model CM3. *J. Climate*, **24**, 3484-3519, doi: 10.1175/2011JCLI3955.1.

Held, I. M., T. L. Delworth, J. Lu, K. L. Findell, and T. R. Knutson, 2005: Simulation of Sahel drought in the 20th and 21st centuries. *Proc. Natl. Acad. Sci.*, **102**, 17891-17896.

Hoerling, M., and A. Kumar, 2003: The perfect ocean for drought. *Science*, **299**, 691–694.

Horel, J. D., and J. M. Wallace, 1981: Planetary-scale atmospheric phenomena associated with the Southern Oscillation. *Mon. Wea. Rev.*, **109**, 813–829.

Jia, L., and T. DelSole, 2011: Diagnosis of multiyear predictability on continental scales. *J. Climate*, **24**, 5108–5124.

Keenlyside, N. S., M. Latif, J. Jungclaus, L. Kornblueh, and E. Roeckner, 2008: Advancing decadal-scale climate prediction in the North Atlantic sector. *Nature*, **453**, 84-88.

Latif, M., T. Martin, and W. Park, 2013: Southern Ocean sector centennial climate variability and recent decadal trends. *J. Climate*, **26**, 7767–7782, doi:10.1175/JCLI-D-12-00281.1.

Martin, T., W. Park and M. Latif, 2013: Multi-centennial variability controlled by Southern Ocean convection in the Kiel Climate Model. *Clim. Dyn.*, **40**, 2005-2022.

Msadek, R., and Coauthors, 2014: Predicting a decadal shift in North Atlantic climate variability using the GFDL forecast system. *J. Climate*, **27**, 6472-6496.

Meehl, G. A., and H. Teng, 2012: Case studies for initialized decadal hindcasts and predictions for the Pacific region. *Geophys. Res. Lett.*, **39**, L22705, doi:10.1029/2012GL053423.

Mo, K. C., and R. W. Higgins, 1997: The Pacific–South American mode and tropical convection during the Southern Hemisphere winter. *Mon. Wea. Rev.*, **126**, 1581–1596.

Mochizuki, T., and Coauthors, 2010: Pacific decadal oscillation hindcasts relevant to near-term climate prediction. *Proc. Natl. Acad. Sci.*, **107**, 1833-1837.

Newman, M., 2007: Interannual to decadal predictability of tropical and North Pacific sea surface temperatures. *J. Climate*, **20**, 2333-2356.

Polvani, L. M., and K. L. Smith, 2013: Can natural variability explain observed Antarctic sea ice trends? New modeling evidence from CMIP5. *Geophys. Res. Lett.*, **40**(12), 3195–3199, doi: 10.1002/grl.50578.

Pohlmann, H., M. Botzet, M. Latif, A. Roesch, M. Wild, and P. Tschuck, 2004: Estimating the decadal predictability of a coupled AOGCM. *J. Climate*, **17**, 4463–4472.

Purkey, S. G., and G. C. Johnson, 2010: Warming of global abyssal and deep Southern Ocean waters between the1990s and 2000s: Contributions to global heat and sea level rise budgets. *J. Climate*, **23**, 6336–6351.

Purkey, S. G., and G. C. Johnson, 2012: Global contraction of Antarctic Bottom Water between the 1980s and 2000s. *J. Climate*, **25**, 5830–5844.

Purich, A., W. Cai, M. H. England and T. Cowan, 2016: Evidence for link between modelled trends in Antarctic sea ice and underestimated westerly wind changes. *Nature Communications*, **7**, 10409, doi:10.1038/ncomms10409.

Robson, J. I., R. T. Sutton, and D. M. Smith, 2012: Initialized decadal predictions of the rapid warming of the North Atlantic Ocean in the mid 1990s. *Geophys. Res. Lett.*, **39**, L19713, doi:10.1029/2012GL053370.

Smith, T. M., and R. W. Reynolds, 2004: Improved extended reconstruction of SST (1854-1997). *J. Climate*, **17**, 2466-2477.

Smith, D. M., S. Cusack, A. W. Colman, C. K. Folland, G. R. Harris, and J. M. Murphy, 2007: Improved surface temperature prediction for the coming decade from a global climate model. *Science*, **317**, 796-799.

Wang, G., and D. Dommenget, 2016: The leading modes of decadal SST variability in the Southern Ocean in CMIP5 simulations. *Clim. Dyn.*, **47**, 1775-1792.

Yang, X., and Coauthors, 2013: A predictable AMO-like pattern in the GFDL fully coupled ensemble initialized and decadal forecasting system. *J. Climate*, **26**, 650-661.

Yeager, S. G., A. Karspeck, G. Danabasoglu, J. Tribbia, and H. Teng, 2012: A decadal prediction case study: Late twentieth-century North Atlantic Ocean heat content. *J. Climate*, **25**, 5173–5189.

Zunz, V., H. Goosse, and F. Massonnet, 2013: How does internal variability influence the ability of CMIP5 models to reproduce the recent trend in Southern Ocean sea ice extent? *Cryosphere*, **7**, 451-468.

Zanna, L., P. Heimbach, A. M. Moore, and E. Tziperman, 2012: Upper-ocean singular vectors of the North Atlantic climate with implications for linear predictability and variability. *Quart. J. Roy. Meteor. Soc.*, **138**, 500–513, doi:10.1002/qj.937.

Zhang, L., L. W, and J. Zhang, 2011: Simulated response to recent freshwater flux change over the gulf stream and its extension: coupled Ocean-Atmosphere adjustment and Atlantic-Pacific Teleconnection. *J. Climate.*, **24**(15), 3971-3988.

Zhang, L., and T. L. Delworth, 2015: Analysis of the characteristics and mechanisms of the Pacific Decadal Oscillation in a suite of coupled models from the Geophysical Fluid Dynamics Laboratory. *J. Climate*, **28**, 7678–7701.

Zhang, L., and T. L. Delworth, 2016: Simulated response of the Pacific decadal oscillation to climate change. *J. Climate*, **29**, 5999–6018.

Zhang, L., T. L. Delworth and F. Zeng, 2016: The impact of multidecadal Atlantic meridional overturning circulation variations on the Southern Ocean. *Clim. Dyn.*, doi:10.1007/s00382-016-3190-8.

Zhang, L., and T. L. Delworth 2016: Impact of the Antarctic bottom water formation on the Weddell Gyre and its northward propagation characteristics in GFDL model. *Journal of Geophysical Research: Oceans*, **121**(8), 5825-5846.

Figure Captions:

Figure 1: Spatial patterns of potential predictability variance fraction (ppvf) for 5-yr (a), 11-yr (b) and 25-yr (c) mean SST in GFDL CM2.1 control run.

Figure 2: The leading predictable component (APT1) of Southern Ocean (SO) SST in GFDL CM2.1 model. (a) Spatial pattern (^{o}C). (b) Normalized time series. (c) Power spectrum of time series (black line). The blue line denotes the 90% confidence level based on red noise null hypothesis (d) Squared multiple correlation coefficients R^2. The dashed black line denotes the 95% significance level.

Figure 3: Same as Figure 2 but for the second most predictable component (APT2).

Figure 4: (a) Coherence of the APT1 and APT2 time series. The black line denotes the 95% confidence level. (b) Lead lag correlation between the APT1 and APT2 time series. The positive (negative) lags means the APT1 leads (lags). The yellow points imposed on the bars denote the correlation is significant at 95% level.

Figure 5: Regression of (a) mixed layer depth (m, shading)/ net heat flux (Contour interval is 1W/m^2. Black solid lines denote the atmosphere heating the ocean, while the grey dash lines denote the ocean losing heat to the atmosphere), (b) global meridional overturning circulation (GMOC, Sv), (c) zonal mean (0^{o}-360^{o}E) temperature (^{o}C) and (d) sea ice concentration (100%)/surface wind (m/s) upon the normalized APT1 time series. Shown are only regions where the regression is significant at 95% confidence level.

Figure 6: Same as Figure 5 but upon the normalized APT2 time series.

Figure 7: Characteristics of internal deep convection over the SO in GFDL CM2.1 model. (a) Long term mean GMOC (Sv). Red (blue) color denotes clockwise (anti-clockwise) cell. (b) Normalized time series of Antarctic Bottom Water (AABW) Cell index which is defined as the minimum value of GMOC value south of 60^{o}S. (c) Power spectrum of AABW cell index. (d) Lead lag correlation between the AABW cell index and the most predictable component of SO SST (APT1). Positive (negative) lags mean the AABW cell leads (lags) the APT1.

Figure 8: Lagged regression of GMOC anomalies against the normalized AABW cell index in GFDL CM2.1 model. Unit is Sv. All data are 10-yr averaged before regression. Shown are only regions where the regression is significant at 95% confidence level.

Figure 9: Same as Figure 8 but for the SST (shading) and surface wind stress (vector). Units are ^{o}C for SST and N/m^2 for wind stress.

Figure 10: Same as Figure 8 but for sea ice concentration (100%).

Figure 11: Same as Figure 8 but for zonal mean (0^oE-360^oE) temperature (^oC).

Figure 12: (a) Normalized time series of 30-yr low pass filtered AABW cell strength, Weddell Sea (WS, $75-55^oS$, 52^oW-30^oE) and Southern Ocean (SO, $70-50^oS$, $0-360^oE$) averaged SST anomalies in the fully coupled GFDL CM2.1 control run. Unit is 1. (b) Lead lag correlation between the AABW and SST anomalies averaged over the WS/SO. X-axis denotes lead and lag years.

Figure 13: (a) Time evolution of annual mean ocean temperature anomalies (^oC) averaged over the Weddell Sea (300^o-375^oE, 75^o-55^oS). The temperature anomaly is relative to a composite of 30 years of each of the two major convection periods (year 2950-2980 and year 3020-3050). Meridional profile of temperature anomalies (^oC, shading) and zonal current (contour interval: 10cm/s, black: eastward current, gray: westward current) along 16^oW section before shut down of convection (averaged in year 2960-2980) (b) and during non-convective regime (averaged in year 2990-3100) (c). (d) Horizontal map of the oceanic total column integrated heat content depletion (10^9 J/m^2) associated with the deep convection. The depletion is taken as the difference between 10-year averages from just before and at the end of a convection event. Time series of annual mean oceanic heat content (10^{22} J) over the Weddell Sea for the below (e) and upper (f) 1000m. All data are 10-yr averaged before analysis.

Figure 14: The leading predictable component (GAPT1) of surface air temperature (SAT) over the Antarctic continent. (a) Physical pattern (^oC). (b) Power spectrum of normalized GAPT1 time series. (c) Squared multiple correlation coefficients R^2. (d) Regression of global SST against the normalized GAPT1 time series (^oC).

Figure 15: Same as Figure 13 but for the precipitation (mm/day) over the Antarctic continent.

Figure 16: The APT decomposition of SO SST in the CM3 model. Spatial patterns of the most (APT1, a) and second most (APT2, b) predictable components. (c) Power spectrum of APT1 and APT2 time series. Red (blue) dash line denotes the 90% significance level for the APT1 (APT2) spectrum. Squared multiple correlation coefficients R^2 and squared persistence for the APT1 (d) and APT2 (e) components. The dashed black line denotes the 95% significance level. (f) Lead lag correlation between the AABW cell index and theAPT1 time series. Positive (negative) lags mean the AABW cell leads (lags) the APT1. The yellow points imposed on the bars denote the correlation is significant at 95% level.

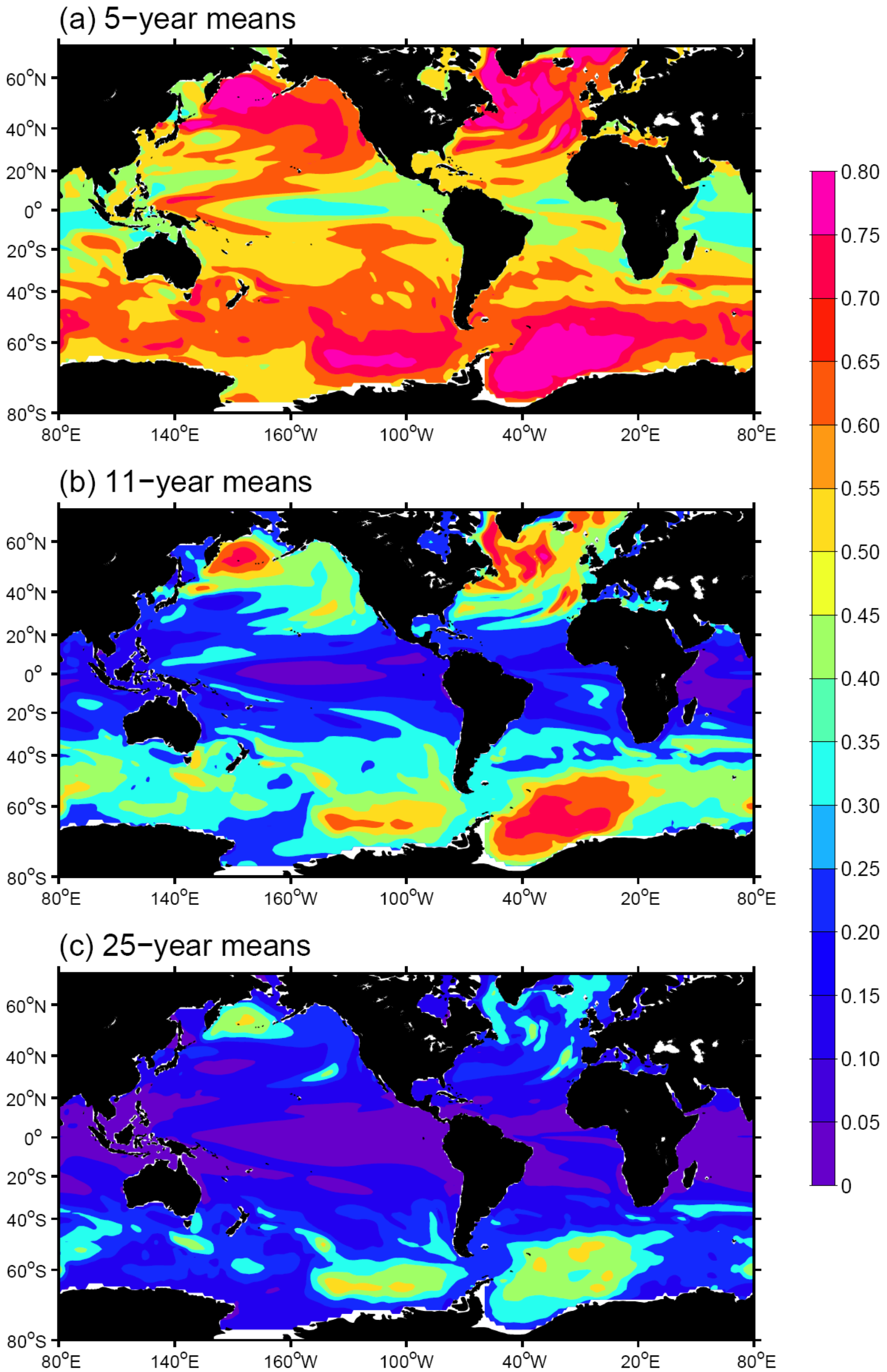

Figure 1: Spatial patterns of potential predictability variance fraction (ppvf) for 5-yr (a), 11-yr (b) and 25-yr (c) mean SST in GFDL CM2.1 control run.

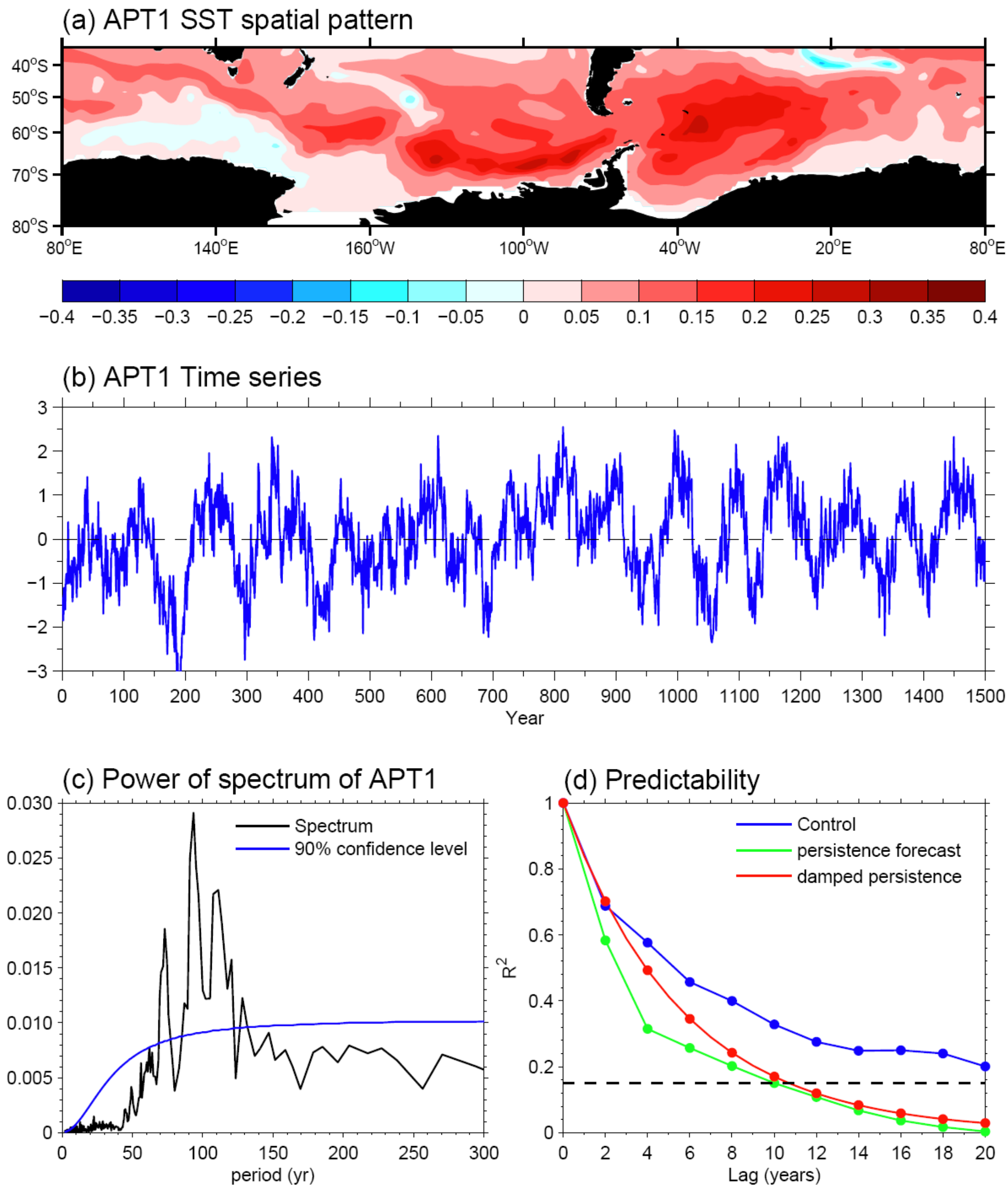

Figure 2: The leading predictable component (APT1) of Southern Ocean (SO) SST in GFDL CM2.1 model. (a) Spatial pattern (°C). (b) Normalized time series. (c) Power spectrum of time series (black line). The blue line denotes the 90% confidence level based on red noise null hypothesis. (d) Squared multiple correlation coefficients R^2. The dashed black line denotes the 95% significance level.

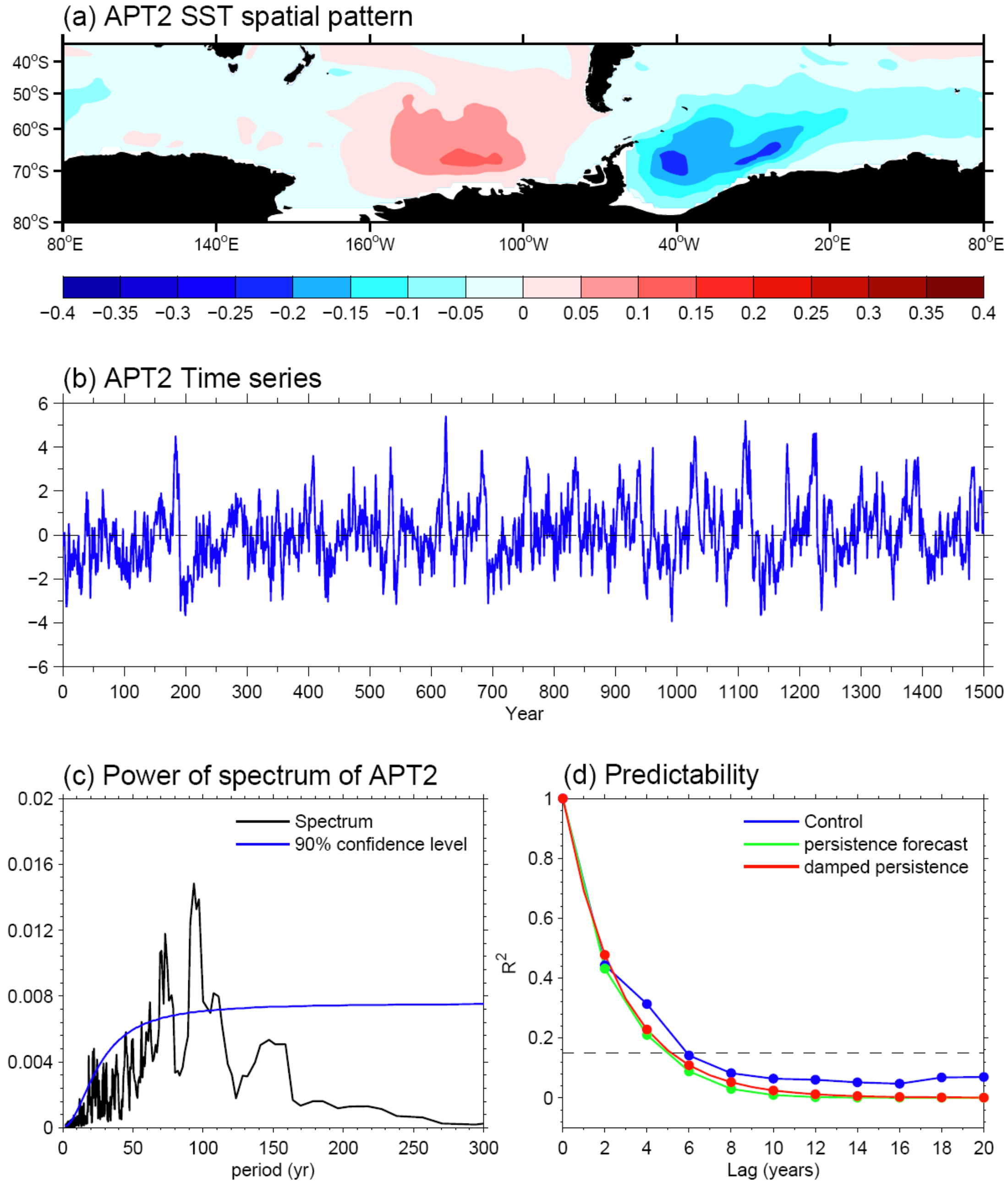

Figure 3: Same as Figure 2 but for the second most predictable component (APT2).

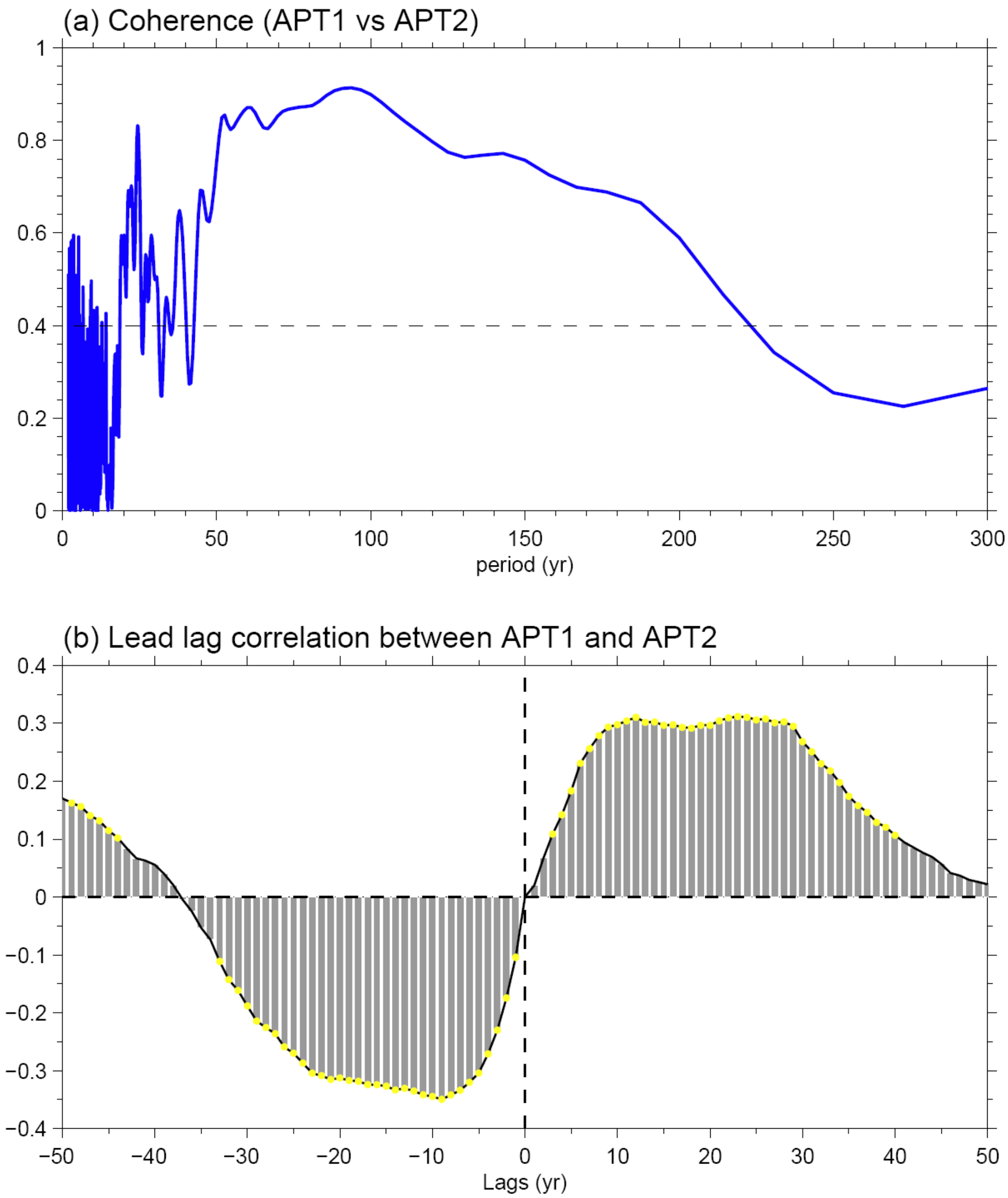

Figure 4: (a) Coherence of the APT1 and APT2 time series. The black line denotes the 95% confidence level. (b) Lead lag correlation between the APT1 and APT2 time series. The positive (negative) lags means the APT1 leads (lags). The yellow points imposed on the bars denote the correlation is significant at 95% level.

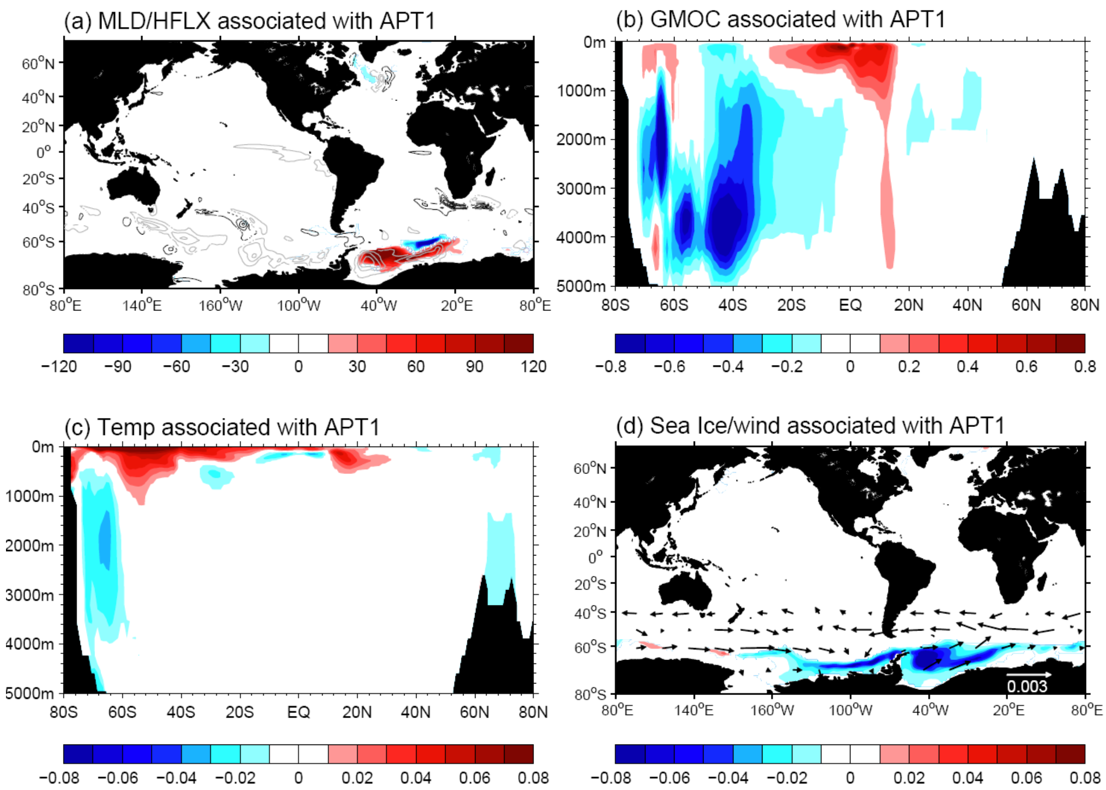

Figure 5: Regression of (a) mixed layer depth (m, shading)/ net heat flux (Contour interval is $1W/m^2$. Black solid lines denote the atmosphere heating the ocean, while the grey dash lines denote the ocean losing heat to the atmosphere), (b) global meridional overturning circulation (GMOC, Sv), (c) zonal mean (0^{o}-360^{o}E) temperature (^{o}C) and (d) sea ice concentration (100%)/surface wind (m/s) upon the normalized APT1 time series. Shown are only regions where the regression is significant at 95% confidence level.

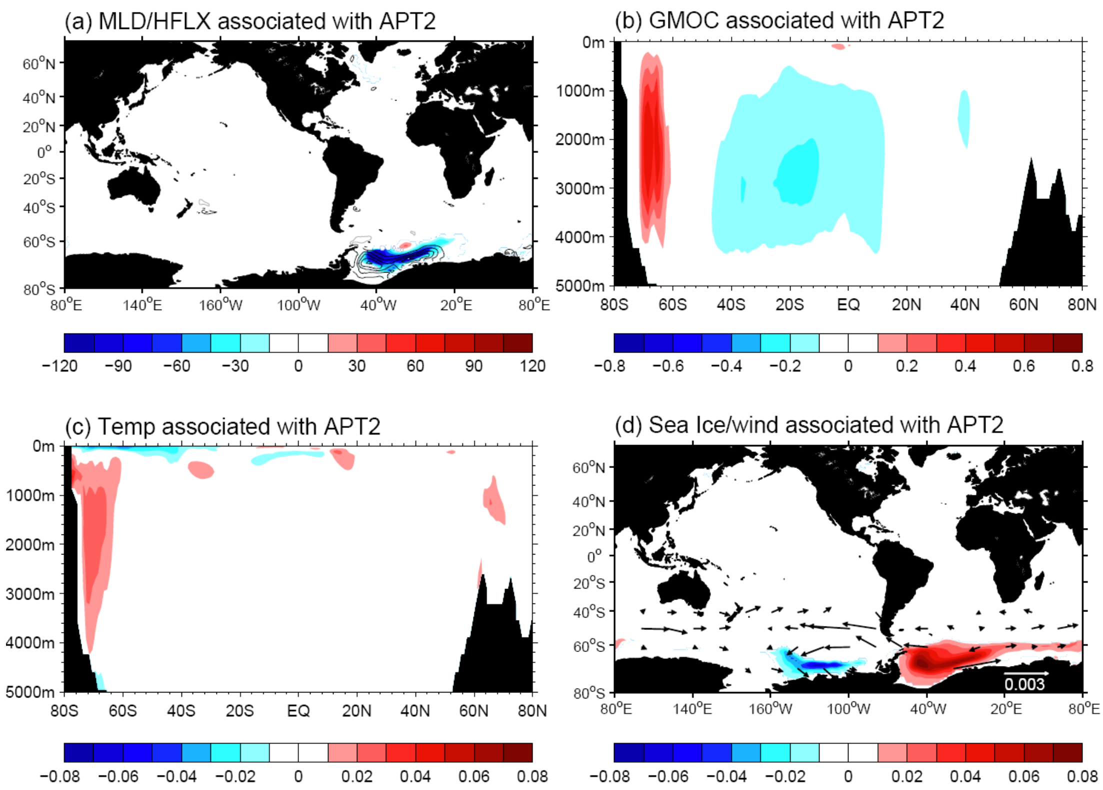

Figure 6: Same as Figure 5 but upon the normalized APT2 time series.

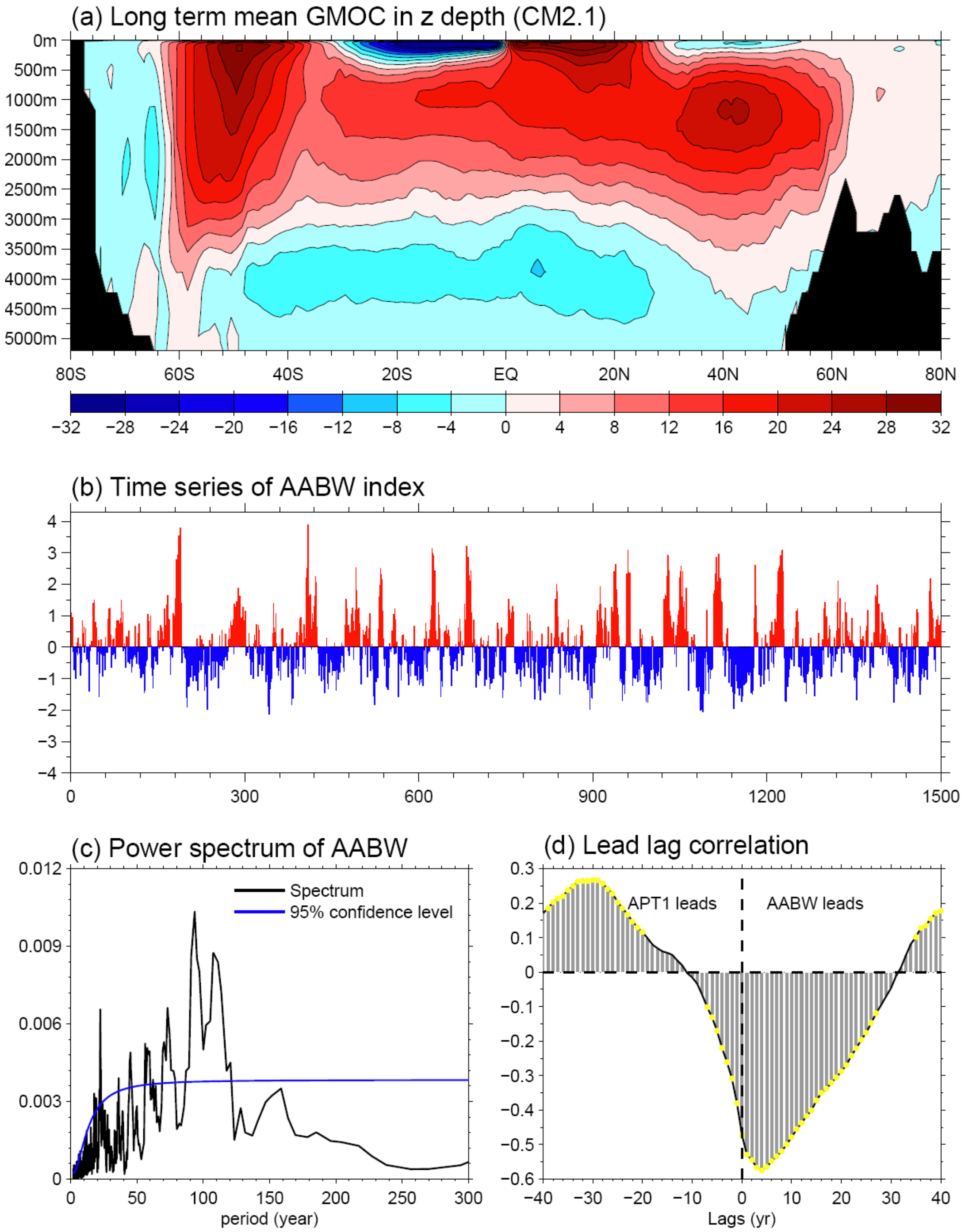

Figure 7: Characteristics of internal deep convection over the SO in GFDL CM2.1 model. (a) Long term mean GMOC (Sv). Red (blue) color denotes clockwise (anti-clockwise) cell. (b) Normalized time series of Antarctic Bottom Water (AABW) Cell index which is defined as the minimum value of GMOC value south of 60^{o}S. (c) Power spectrum of AABW cell index. (d) Lead lag correlation between the AABW cell index and the most predictable component of SO SST (APT1). Positive (negative) lags mean the AABW cell leads (lags) the APT1.

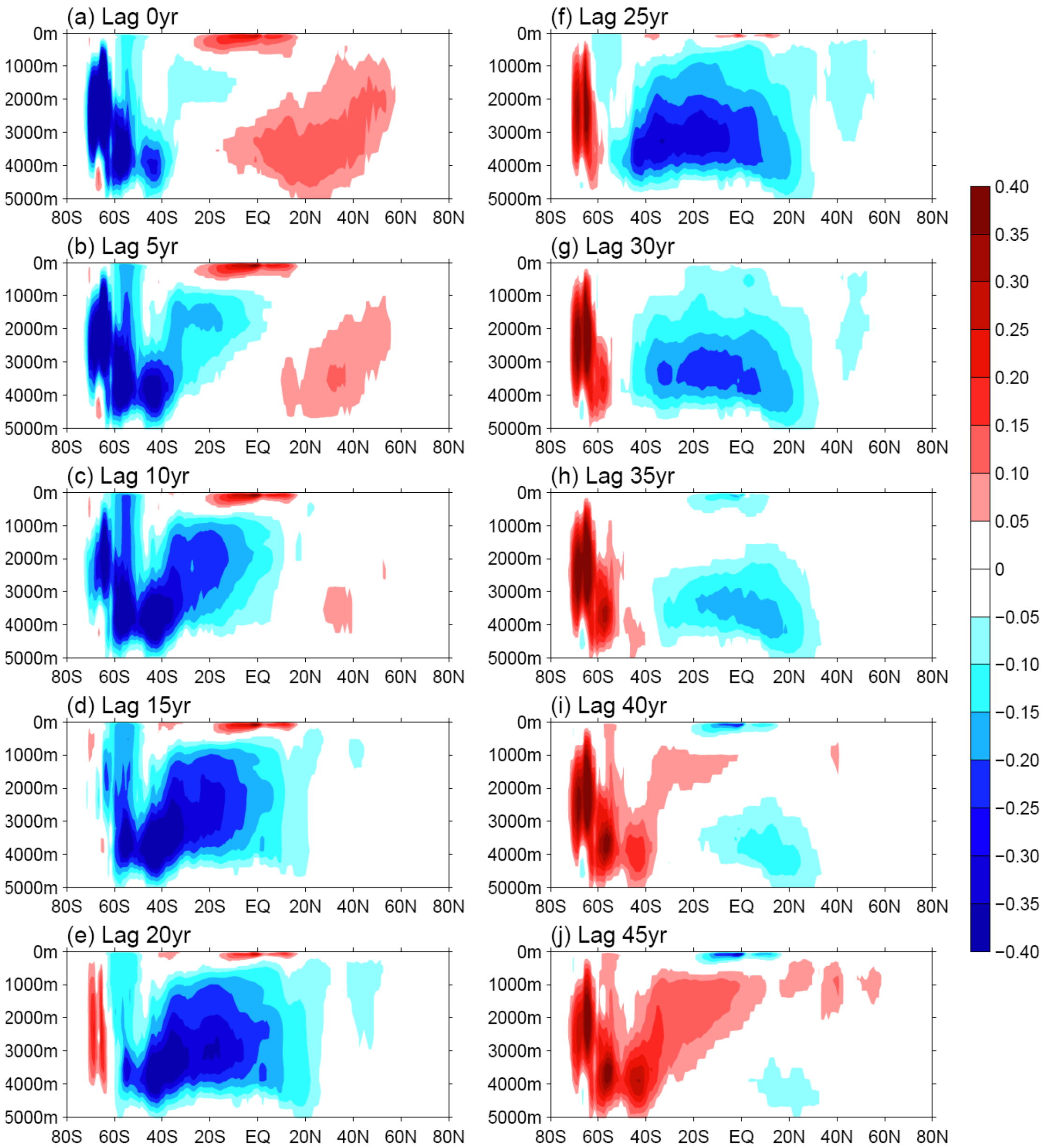

Figure 8: Lagged regression of GMOC anomalies against the normalized AABW cell index in GFDL CM2.1 model. Unit is Sv. All data are 10-yr averaged before regression.

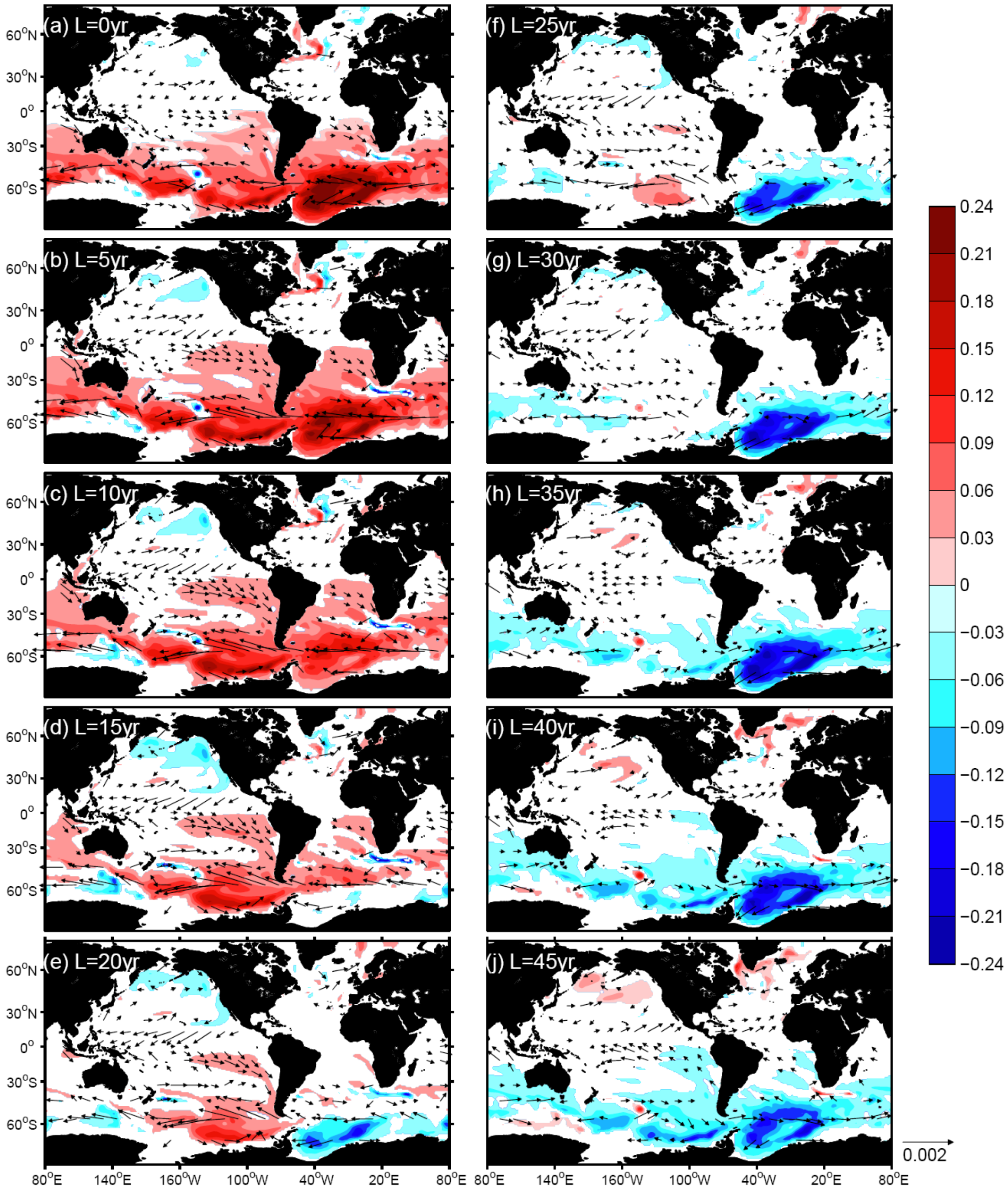

Figure 9: Same as Figure 8 but for the SST (shading) and surface wind stress (vector). Units are ^{o}C for SST and N/m^2 for wind stress.

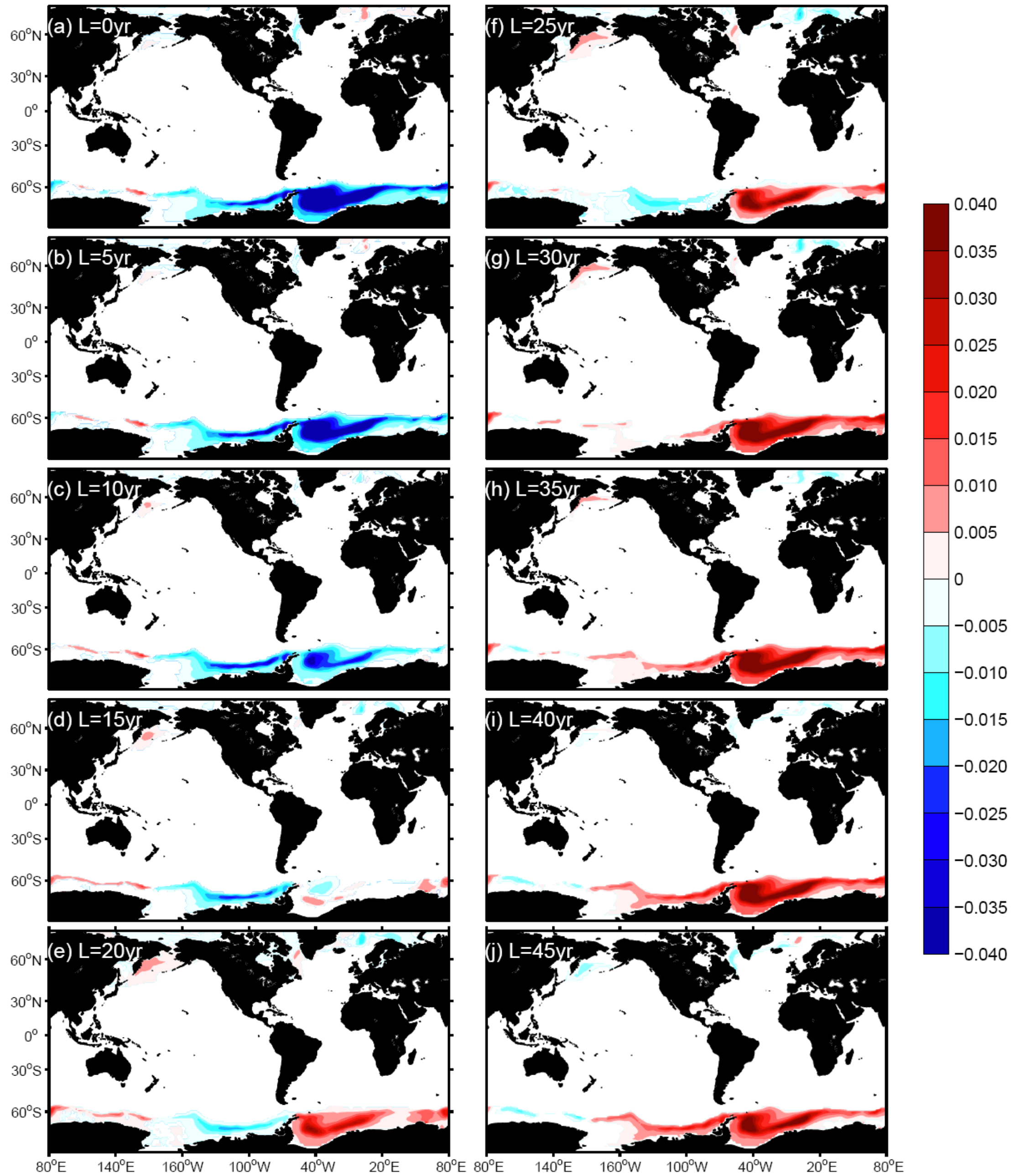

Figure 10: Same as Figure 8 but for sea ice concentration (100%).

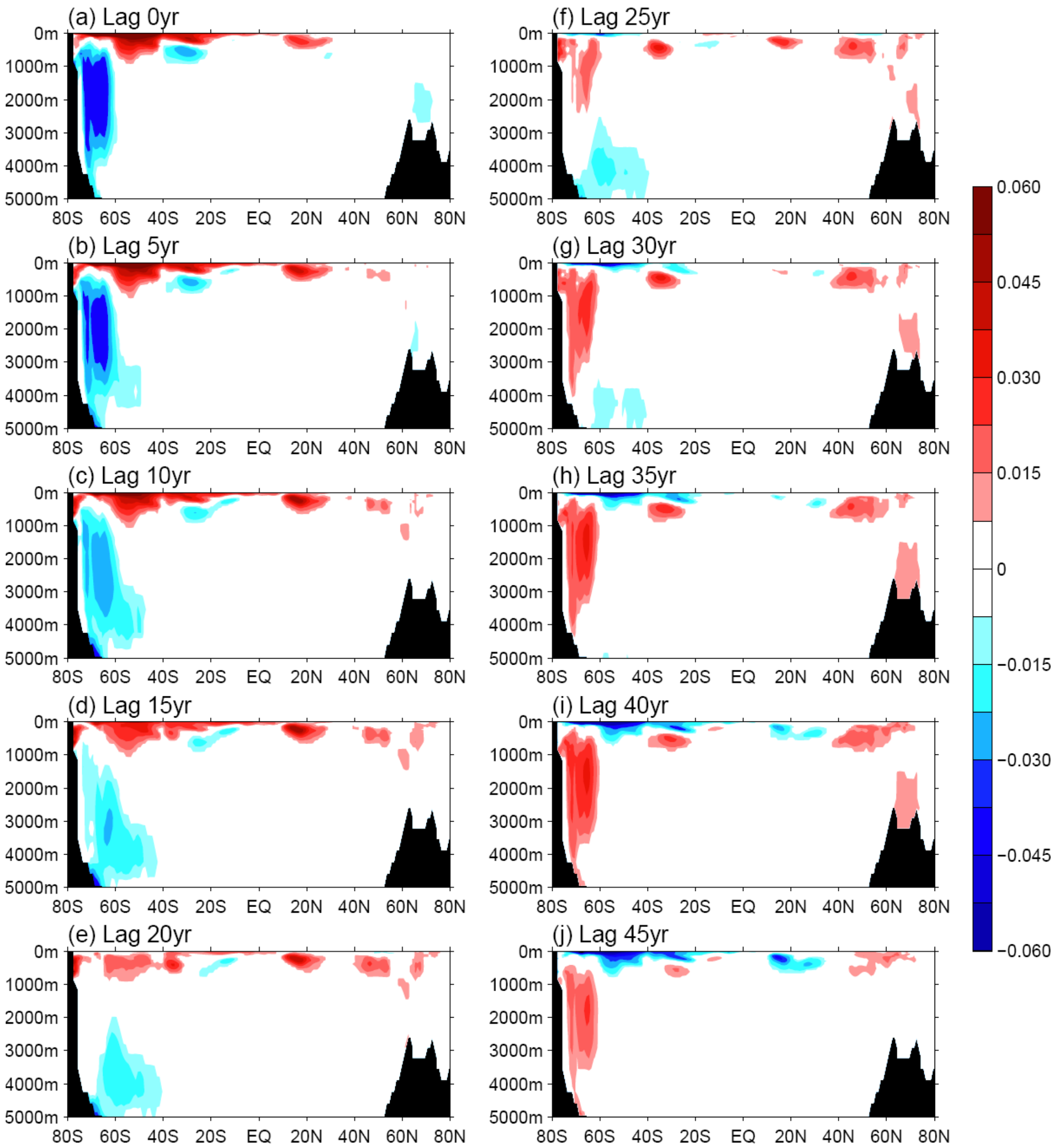

Figure 11: Same as Figure 8 but for zonal mean (0^{o}E-360^{o}E) temperature (^{o}C).

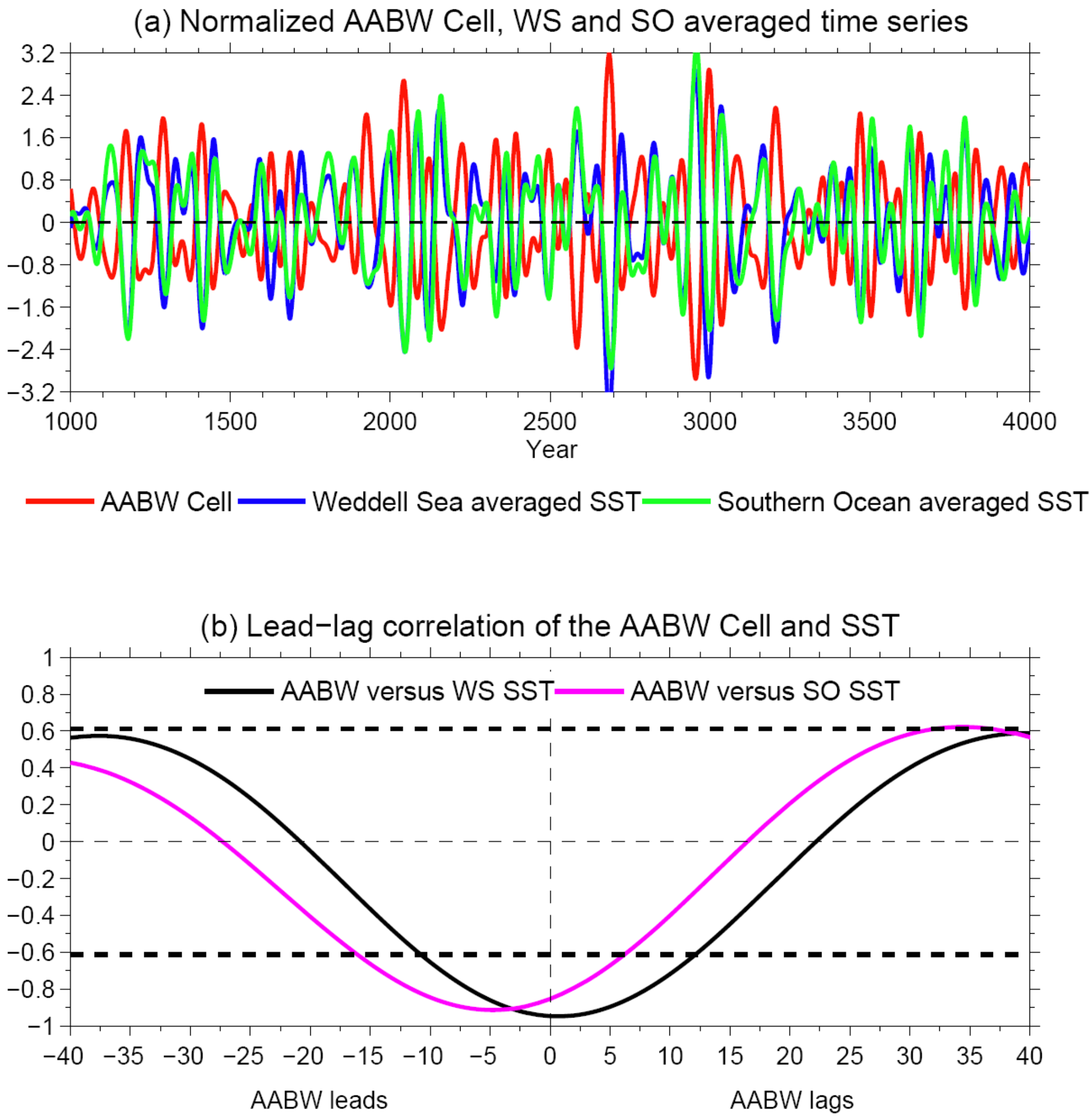

Figure 12: (a) Normalized time series of 30-yr low pass filtered AABW cell strength, Weddell Sea (WS, 75-55°S, 52°W-30°E) and Southern Ocean (SO, 70-50°S, 0-360°E) averaged SST anomalies in the fully coupled GFDL CM2.1 control run. Unit is 1. (b) Lead lag correlation between the AABW and SST anomalies averaged over the WS/SO. X-axis denotes lead and lag years.

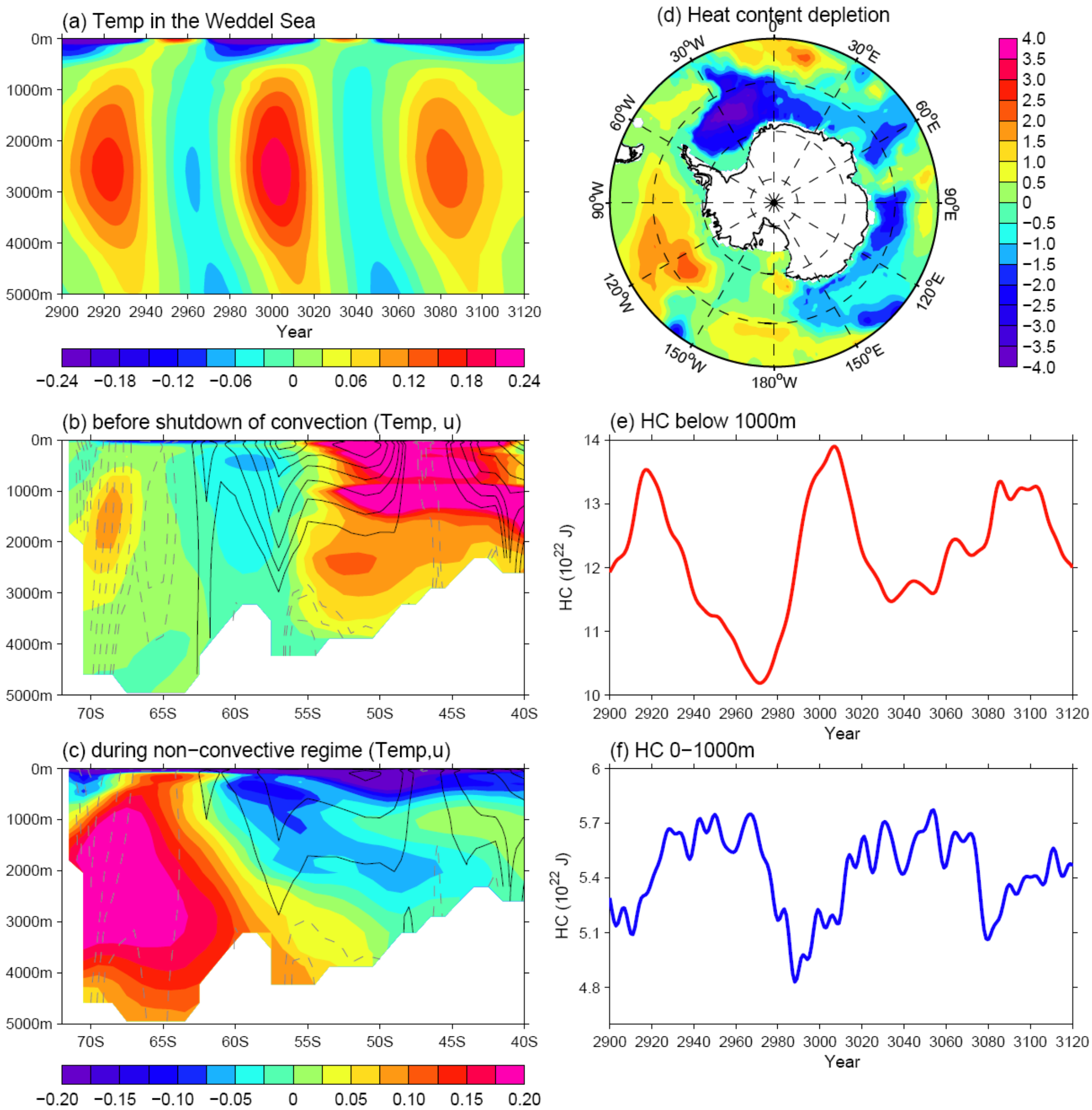

Figure 13: (a) Time evolution of annual mean ocean temperature anomalies (^{o}C) averaged over the Weddell Sea (300^{o}-375^{o}E, 75^{o}-55^{o}S). The temperature anomaly is relative to a composite of 30 years of each of the two major convection periods (year 2950-2980 and year 3020-3050). Meridional profile of temperature anomalies (^{o}C, shading) and zonal current (contour interval: 10cm/s, black: eastward current, gray: westward current) along 16^{o}W section before shut down of convection (averaged in year 2960-2980) (b) and during non-convective regime (averaged in year 2990-3100) (c). (d) Horizontal map of the oceanic total column integrated heat content depletion (10^{9} J/m^{2}) associated with the deep convection. The depletion is taken as the difference between 10-year averages from just before and at the end of a convection event. Time series of annual mean oceanic heat content (10^{22} J) over the Weddell Sea for the below (e) and upper (f) 1000m. All data are 10-yr averaged before analysis.

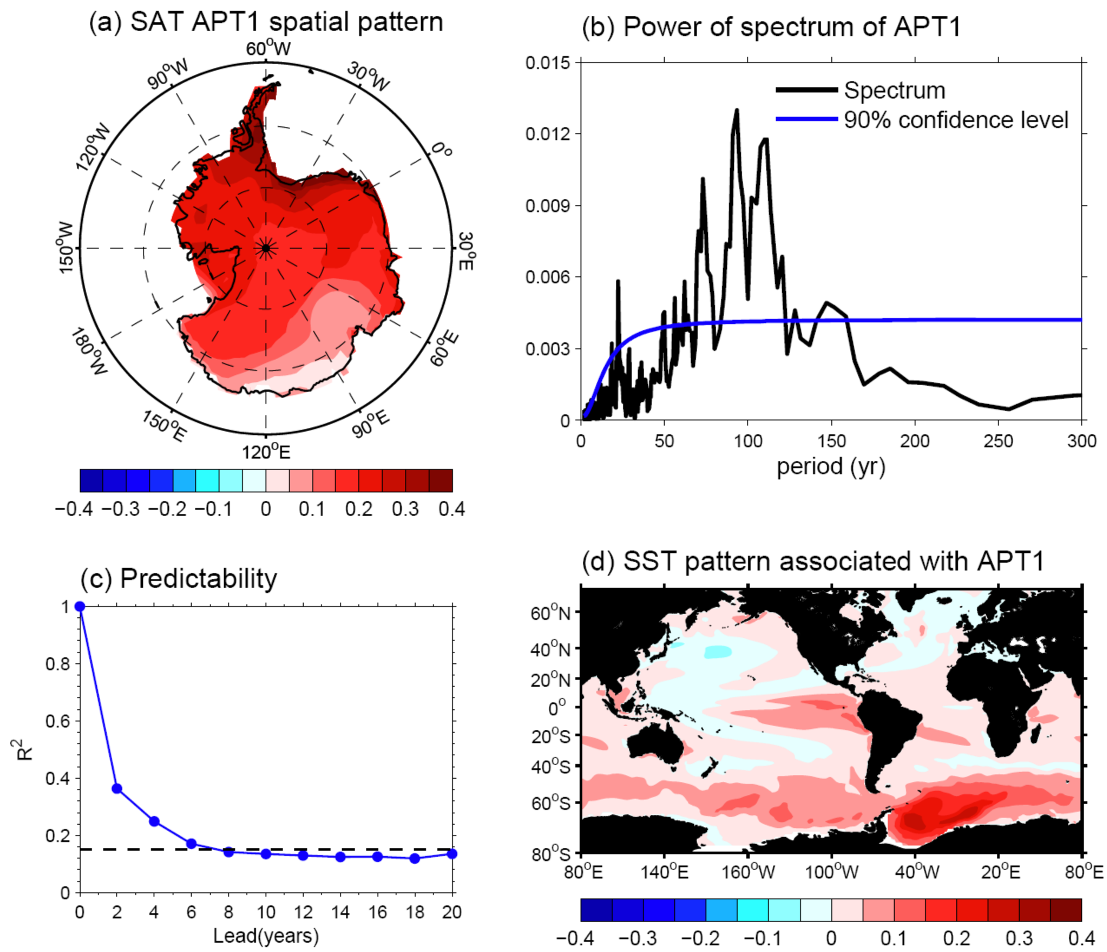

Figure 14: The leading predictable component (GAPT1) of surface air temperature (SAT) over the Antarctic continent. (a) Physical pattern (°C). (b) Power spectrum of normalized GAPT1 time series. (c) Squared multiple correlation coefficients R^2. (d) Regression of global SST against the normalized GAPT1 time series (°C).

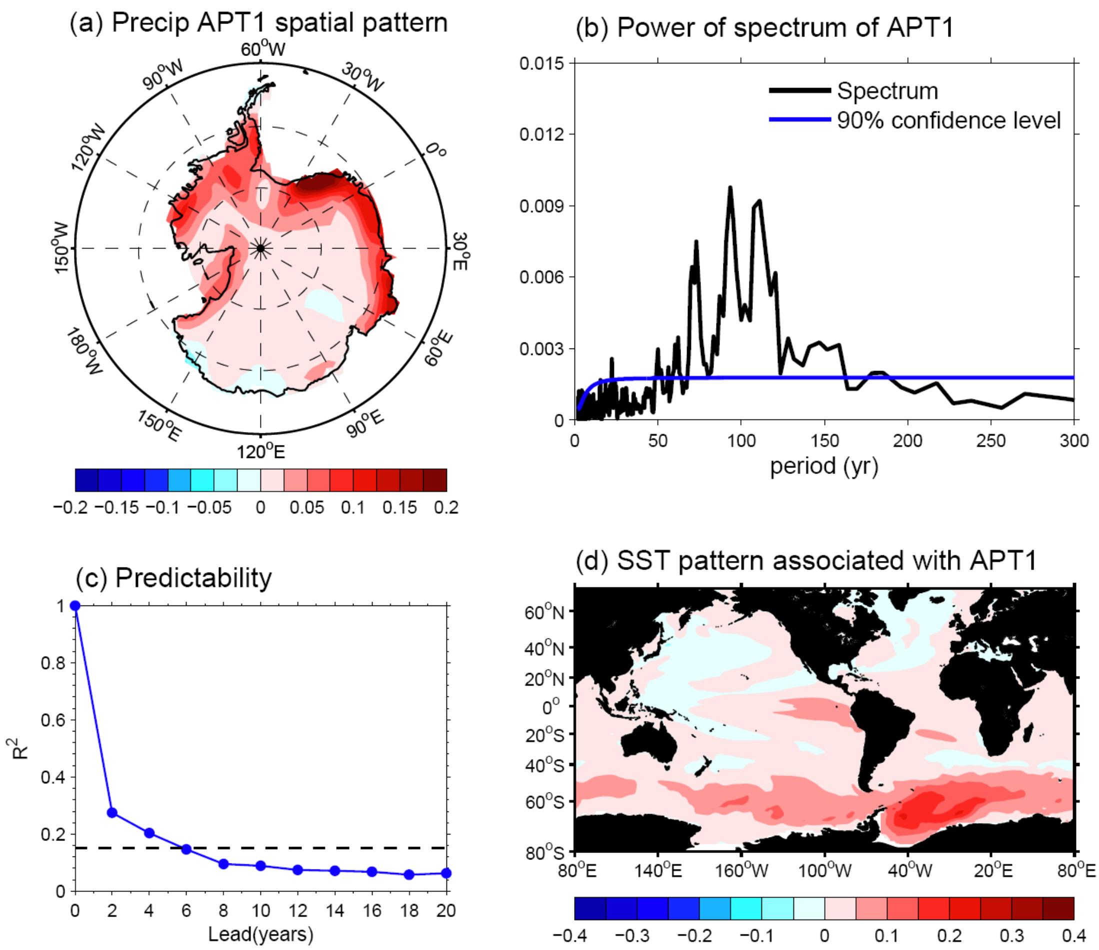

Figure 15: Same as Figure 14 but for the precipitation (mm/day) over the Antarctic continent.

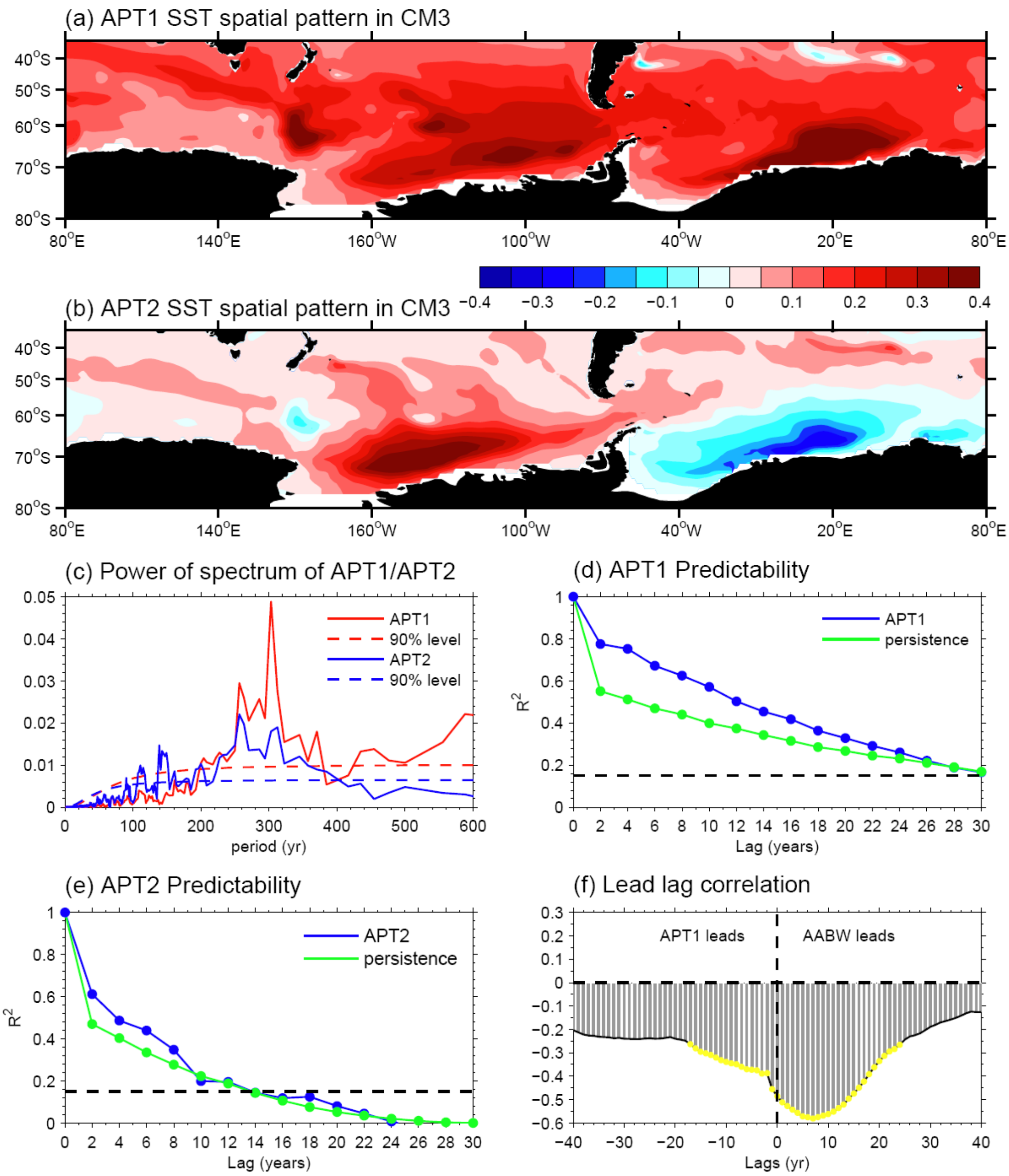

Figure 16: The APT decomposition of SO SST in the CM3 model. Spatial patterns of the most (APT1, a) and second most (APT2, b) predictable components. (c) Power spectrum of APT1 and APT2 time series. Red (blue) dash line denotes the 90% significance level for the APT1 (APT2) spectrum. Squared multiple correlation coefficients R^2 and squared persistence for the APT1 (d) and APT2 (e) components. The dashed black line denotes the 95% significance level. (f) Lead lag correlation between the AABW cell index and theAPT1 time series. Positive (negative) lags mean the AABW cell leads (lags) the APT1. The yellow points imposed on the bars denote the correlation is significant at 95% level.